The Dissertation Committee for Elliot Jeremy Hans Dahl
certifies that this is the approved version of the following dissertation:

Viscoelastic wave propagation along a borehole using squirt flow and Biot poroelastic theory

Committee:

Kyle Spikes, Supervisor

Carlos Torres-Verdin

Mrinal Sen

David Mohrig

Hugh Daigle

Viscoelastic wave propagation along a borehole using squirt flow and Biot poroelastic theory

by

Elliot Jeremy Hans Dahl

DISSERTATION

Presented to the Faculty of the Graduate School of

The University of Texas at Austin

in Partial Fulfillment

of the Requirements

for the Degree of

DOCTOR OF PHILOSOPHY

THE UNIVERSITY OF TEXAS AT AUSTIN

December 2017

Dedicated to my family and my Guddu.

Acknowledgments

I want to give a special thanks to my advisor, Dr. Kyle Spikes. I am extremely grateful for all the help he has provided me with during my PhD. His door was always open. Questions ranging from implementation of Bessel functions to travel grant forms, he never made me feel like any question was to dumb to ask. He has evolved from being an advisor to a personal friend.

Thanks to Dr. Carlos Torres-Verdin who let me partake in his group meetings and borrow his code. It has provided me with very valuable knowledge and pushed me in the right direction. I would also like to thank Dr. Nicola Tisato whose knowledge of various dispersion mechanisms and espresso making has made my research even better. My gratitude goes to my dissertation committee members, Dr. Mrinal Sen, Dr. David Mohrig and Dr. Hugh Daigle for their time, support and help with this research.

I would like to thank our graduate coordinator Philip Guerro, who was a great help in understanding which forms to fill out, what deadlines where present and who UTs volleyball team were playing next.

I would also like to thank Dr. Ruijia Wang, Dr. Kelvin Amalowku, Dr. Giorgos Papageorgiou, for valuable help and discussions.

I am grateful to many present and past researchers and students in our department. My thanks goes to Thomas Hess, Peter Nelson, David Tang,

Chris Linick, Barry Borgman, Andrew Yanke, Qi Ren, Sarah Coyle, Jacqueline Maleski, Russell Cater, Meijuan Jiang, Han Liu, Lauren Becker, Makoto Sadahiro, Karl Oskar Sletten, Kelly Regimbal, Wei Xie and Micheal McCann for making my stay here a lot more fun and interesting!

Last but not least, I would like to thank my girlfriend Florence Navarro and my family, for their love and support. They make my life so much richer! A special thanks to my father Dr. Jeremy Dahl who keeps helping me with everything from language edits to career suggestions.

Viscoelastic wave propagation along a borehole using squirt flow and Biot poroelastic theory

Elliot Jeremy Hans Dahl, Ph.D.
The University of Texas at Austin, 2017

Supervisor: Kyle Spikes

Observations of seismic waves provide valuable understanding of Earth subsurface properties. These measurements are used to study large-scale subsurface features, kilometers in width, borehole-scale situations, meters of interest, and with core samples, a few centimeters in length. A common practice is to assume that the elastic rock-properties (P- and S-wave velocities) are the same for all frequencies. This is why sonic logs without corrections, for example, are used to constrain velocity models that transform seismic data from time to depth and to calibrate rock physics models used in seismic inversion to link elastic properties to reservoir properties. However, when seismic waves propagate in Earth materials, they are subject to different dispersion mechanisms, which makes the velocities frequency dependent. Understanding these effects on acoustic wave propagation can improve our models that constrain the subsurface and ultimately give us better hydrocarbon predictability.

The main objective of this dissertation is to contribute to the understanding of how fluid in the pore space affects acoustic wave propagation. To

achieve this goal, I first developed a frequency-dependent wave equation that accounts for local (squirt) and global (Biot) flow. The new model is tested against other squirt-Biot flow theories for both synthetic cases and utrasonic velocity data. I find the developed model to be consistent with the compared models in the synthetic cases. For the utrasonic velocity data, I find predictions from the new model to be closest to the measured data.

In the second part of the dissertation, I use the developed squirt-Biot flow wave equation to simulate wave propagation in fluid-filled boreholes containing formations with different quantities of compliant pores. These are compared with formations where no compliant pores are present. I use the discrete wavenumber summation method with both a monopole and a dipole source to generate the wave fields. I find that fluid-saturated compliant pores can significantly affect the effective formation P- and S-wave velocities. This in turn affects the various acoustic wave modes causing increasing dispersion and attenuation. Thus, knowledge of the micro-scale structure of the fluid-saturated rock is of importance for understanding the acoustic waveforms and the dispersive behavior of the various modes. Depending on the locations where the critical frequencies for the different dispersion mechanisms occurs, acoustic velocity estimates can differ from the seismic-frequency velocities. Having a frequency dependent model accounting for the various dispersion mechanisms can help better connect the various velocity measurements and ultimately serve to give us an even more realistic picture of the subsurface.

Table of Contents

List of Tables

List of Figures

Chapter 1

Introduction

1.1 Motivation and objectives

Subsurface rock formations targeted by exploration can have similar solid composition, fluid type and total amount of porosity but respond completely different to seismic wave propagation. Different characteristics of the rock, i.e., pore shape, grain size and permeability together with the mobile fluids can lead to various velocity changes in the effective formation. Borehole acoustic wave velocity measurements are widely used in petroleum reservoir exploration, marine geophysics, reserve estimation, hydrocarbon production and well completions. Sonic logs constrain the velocity models that transform seismic data from time to depth. Another common use is to understand the mechanical properties of a formation, which are important for well completion and production. Mechanical properties of the formation provide information to estimate borehole stability and to understand where to hydraulically fracture the rock. Sonic logs have also been used extensively in rock physics to describe the relationships between the elastic properties (P- and S-wave velocities) and reservoir properties such as lithology, porosity, and saturation. However, most of the conclusions made based on sonic logs do not account for how the rock was structurally arranged and if mobile fluids were present in

the formation or not.

When seismic waves propagate through earth materials, they are subject to attenuation and dispersion from the seismic frequency range to ultrasonic frequencies (Mavko et al., 2009; Müller et al., 2010). A variety of different attenuation and dispersion mechanisms exist, such as geometric dispersion and scattering attenuation where the total energy field is considered conserved. However, most subsurface formations of interest to exploration have fluid-saturated pore space that contain mobile fluids leading to the dispersion mechanisms commonly known as wave-induced fluid flow (WIFF). WIFF leads to inelastic dissipation, where kinetic energy is transferred to heat. As the seismic wave propagates through a fluid-saturated, permeable rock, fluid pressure gradients arise due to internal friction. The WIFF resulting from pressure gradients on the wave length scale is often referred to as macroscopic or global flow. Global flow has theoretically been described by Biot's theory of poroelasticity (Biot, 1956a,b). Biot's equations were derived using a Lagrangian viewpoint with the generalized coordinates given by the six average displacement components of the solid and the fluid (Biot, 1956a). The idealization Biot makes about the porous medium is that the rock is considered homogeneous and isotropic. Only one type of fluid is present in the pore space. The relative motion between fluid and solid is described by Darcy's law, and finally, the wavelength of the passing seismic wave is much larger then the grains or pores in the considered medium. Many studies have investigated the effect of Biot dispersion and attenuation on acoustic waveforms in boreholes (e.g.,

Rosenbaum, 1974; Schmitt, 1988a,d, 1989; Tang and Cheng, 2004; He et al., 2013). These show that the Stoneley wave which is a borehole interface wave is sensitive to the in situ mobility of the saturated porous formation when using a monopole source. The P- and S-wave modes together with the flexural wave mode excited with a monopole and dipole source, respectively, are not found to be influenced by Biot flow to a significant extent.

The assumption Biot makes about uniform pore space limits the theory to very simple rocks, which also explains why the theory has failed in instances to explain dispersion in ultrasonic measurements (Coyner, 1977; Winkler, 1985; Dvorkin and Nur, 1993; Dvorkin et al., 1994). Granular rocks, such as for example sandstone, often contain compliant pores between adjacent grains together with stiffer intergranular pores. When seismic waves propagate through a dual-porosity medium containing stiff and compliant pores, unequal deformation of stiff versus compliant pores produce local pressure gradients. When the frequencies are high enough, the fluid in the compliant pores fail to equilibrate with the surrounding pore fluids, and the rock matrix appears stiffer, contributing to higher seismic velocities. The specific WIFF is referred to as local flow or squirt flow (Mavko and Nur, 1975; Müller et al., 2010). Squirt flow appears to be important in the sonic frequency regime. Both Baron and Holliger (2010) and Sun et al. (2016) model their measured P-wave dispersion in the kHz range successfully with squirt flow models. Furthermore, Sams et al. (2017) found a theoretical squirt-flow model to successfully fit with compared VSP data, sonic log and core velocity dispersion and attenuation measure-

ments from the Imperial College borehole test site, where the inflection point of the P- and S-wave velocity dispersion was in the sonic frequency range.

To the best of my knowledge only two prior studies have investigated the combined effect of squirt and Biot flow on acoustic waveforms, namely Markova et al. (2014) and Chen et al. (2014). Markova et al. (2014) used the Gurevich et al. (2010) simple squirt-flow model to study monopole waveforms. Chen et al. (2014) applied the Tang et al. (2012) cracked porous medium elastic wave theory in a tight formation together with a monopole and dipole source. Both studies find compliant pores to have a significant effect on the various acoustic wave modes.

The main contribution of this dissertation includes development of a unified local- and global flow model that explains the velocity effect of compliant pores on seismic wave propagation. The model is validated through comparison between theoretical estimated ultrasonic velocities and experimental data for two rock types. The model and experimental velocities are similar. With the derived model I simulate waveforms in fluid-filled boreholes surrounded by a rock formation subject to local- and global-flow. Modeling results provide better understanding of the possible effect that compliant pores have on acoustic waveforms in boreholes generated with monopole and dipole sources.

1.2 Chapter description

Chapter 2 establishes a new local- and global-flow model constructed through unification of Chapman et al. (2002) squirt-flow theory together with the classical theory of Biot (1956a,b, 1962a). This model is compared with Gurevich et al. (2010) and Mavko and Jizba (1991) squirt-flow models, where I find the main differences between the models to be a lack of need to estimate the bulk moduli containing only stiff pores, which is used in the theories of Gurevich et al. (2010) and Mavko and Jizba (1991). This parameter requires high-pressure ultrasonic measurements and is very difficult to estimate accurately. The different models are used to predict ultrasonic velocities, which are compared with experimental velocity data as a function of pressure. I find the combined Chapman-Biot flow model predictions to be closest to the actual data measurements.

Chapter 3 investigates the effect of compliant pores, using the unified Chapman-Biot flow model from Chapter 2, on acoustic waveforms in boreholes generated with monopole sources. I use the quasi-analytical method in 1D referred to as the wavenumber summation method (Tang and Cheng, 2004) to generate the wavefields. I study both a fast and a slow formation containing stiff pores and different quantities of micro cracks to be compared with formations with no compliant pores. I use both a 7.5-kHz and a 1-kHz source to investigate the P- and S-wave modes together with the slow-P, guided Stoneley and pseudo-Rayleigh waves. I find that compliant pores can have substantial effects on all the wavemodes. However, the effects are due to changes in ef-

fective formation P- and S-wave velocities rather than to additional fluid-flow mobility. Furthermore, I provide theoretical reasoning as to why it is accurate to exchange the dry moduli with the modified frame moduli derived in Chapter 2 in the theory of Biot to include the effect of squirt flow in the poroelastic theory.

Chapter 4 presents waveforms generated with a dipole source in a fluid-filled borehole surrounded by a slow and fast formation exhibiting local- and global-flow. The waveforms are again generated using the wavenumber summation method. The waveforms are processed with weighted spectral semblance (WSS) (Nolte and Huang, 1997) and compared with the phase-velocity dispersion from solving the period equation (Tang and Cheng, 2004). I find the flexural wave mode to be affected by the presence of compliant pores, in amplitude and phase- and group-velocity dispersion. This result is in agreement from processing the waveforms with WSS and by solving the period equation. Moreover, changing the critical squirt-flow frequency displays the variation in velocity that might be predicted from the low frequency flexural wave-mode in a true formation where knowledge of dispersion mechanisms are difficult to accurately measure.

Chapter 5 discuss the overall conclusions of the dissertation, as well as possible future work.

Chapter 2

Velocity dispersion model for global and local flow

2.1 Abstract

[1] I present a methodology to incorporate squirt flow into the classical theory of Biot. Biot flow explains the wavelength-scale (global) pressure differences whereas squirt flow accounts for the pore-scale (local) pressure gradients affecting the velocities of the fluid-saturated rock. In this work, I derive frequency-dependent dry-rock moduli containing saturated compliant pores, from the theory of Chapman and combine them with the classical theory of Biot to unify the local and global flows. The theory of Chapman is equivalent to Gassmann's and close to Mavko-Jizba's model in the low- and high-frequency regimes when using the explicit expressions for the dry-rock moduli of Chapman. However, the benefit of combining Chapman's theory with Biot's model is the freedom in choosing dry moduli, while also adding the effect of global flow. This enables me to test the unified theory against ultrasonic velocity measurements as a function of effective stress done on Westerley Gran-

[1]Parts of this chapter was first published in Dahl, E.J.H. and K.T.Spikes, "A local and global fluid-effect model for saturated-porous rocks", SEG expanded abstracts, 2017. For this paper I did all the technical work and wrote the manuscript, Kyle reviewed and helped in revisions.

ite and Navajo Sandstone, where dry- and saturated-rock velocities have been measured. I find the combined Biot-Chapman model to perform slightly better then Mavko-Jizba's theory in predicting the observed dispersion. A possible reason for this is the dry-rock bulk moduli without compliant pores, used in the theory of Mavko-Jizba, which is difficult to estimate accurately.

2.2 Introduction

Wave-induced fluid flow (WIFF) is a significant contributor to dispersion and attenuation for passing seismic waves (Müller et al., 2010). As the wave propagates through a fluid-saturated porous medium, pressure gradients appear on a variety of different length scales. The pressure gradients on the seismic-wavelength scale ($10-100$m), with inertial and viscous forces coupling the fluid and the solid movement, can be described by the classical theory of Biot (1956a,b). The resulting WIFF is often times referred to as global or macroscopic flow due to the details of the pore shape and local flow being neglected. This information is instead lumped together in parameters averaged on a scale larger then the typical pore size. However, as shown in Coyner (1977) and Winkler (1985), Biot's theory appears to under predict the dispersion and attenuation in a variety of different ultrasonic velocity measurements as a function of effective stress, with worse predictions for the lower effective stresses. This can be explained with the introduction of compliant or soft pores that close with increasing stress. Compliant pores refer to shapes containing aspect ratios approximately less than 10^{-2} (Shapiro, 2003). These compliant

pores are the main cause for the dispersion mechanism referred to as squirt flow (Mavko and Nur, 1975). When a seismic wave passes through a fluid-saturated porous medium containing stiff and compliant pores, local pressure gradients result due to the unequal deformation of the pore space. Stiff pores deform a lot less than soft pores, stiff pores are considered to have majority shapes with aspect ratios larger than 0.1 (Shapiro, 2003).

If the frequencies in which the wave is propagating are low enough, the fluid in the compliant pores has time to equilibrate with the surrounding pore space. When the frequencies are higher, the fluid becomes trapped, which results in a stiffer rock and higher seismic velocities. This pore-scale WIFF is often referred to as local flow or squirt flow (Müller et al., 2010).

Several theoretical squirt-flow models have been developed to explain the specific velocity dispersion mechanism. Some are based on aspect-ratio distributions (O'Connell and Budiansky, 1977; Palmer and Traviola, 1980), whereas others are built under the assumption of a binary structure of stiff and compliant pores (Chapman et al., 2002; Gurevich et al., 2010). Other attempts also exist to explain global and local flow in a unified theory. Dvorkin and Nur (1993) assume the seismic wave to deform only the fluid-saturated medium in the direction of wave propagation, while allowing the fluid to move in the perpendicular direction as well. This perpendicular fluid flow represents squirt flow. This local-global flow model is unfortunately not consistent with the Gassmann (1951) prediction in the low-frequency regime (Mavko et al., 2009). The reason for this inconsistency is because of the boundary condition

that fluid pressure should vanish on the surface of the representative cylinder, while Gassmann assumes zero fluid pressure at every point in the medium. Pride et al. (2004) used the double-porosity dual-permeability theory of Pride and Berryman (2003a,b) with the assumption of no fluid flow between the principal pore space and the porous grains in order to add the effect of squirt flow to Biot's theory. Sayar and Torres-Verdin (2017) developed an effective medium model which replicates the WIFF effect of Biot (1956a,b) and Chapman et al. (2002), with additional wave-attenuation from acoustic scattering of spherical pores and randomly oriented penny-shaped cracks. Gurevich et al. (2010) used a modified version of Murphy et al. (1986) fluid pressure response in the soft pores combined with the discontinuity formalism of Sayers and Kachanov (1995) to find an unrelaxed frame moduli. This modified frame can be incorporated into Gassmann's or Biot's equations to give either the squirt flow- or combined squirt plus Biot-flow dispersion. This model is equivalent to Gassmann (1951) and Mavko and Jizba (1991) theories in the low- and high-frequency regimes. Mavko and Jizba (1991) quantified the effect of squirt flow using a modified dry frame, where the compliant pores are fluid filled while the stiff pores are dry. Gurevich et al. (2010) and Mavko and Jizba (1991) both incorporate the local pressures into Biot's theory similar to Stoll and Bryan (1969) and Keller (1989), where a viscoelastic frame replaces the dry mineral frame. Although the two theories of Gurevich et al. (2010) and Mavko and Jizba (1991) have shown to be relatively successful in predicting ultrasonic velocity measurements, both use an input parameter, K_h, which is the dry

frame bulk modulus without the compliant pores. This parameter is difficult to estimate, and it is often taken to be the high effective-stress measurement for the dry bulk modulus.

My attempt of incorporating local flow into Biot's model is similar to Stoll and Bryan (1969), Keller (1989) and Gurevich et al. (2010), where I develop frequency-dependent dry-frame moduli to use in both Gassmann's and Biot's theories. I use the theory of Chapman et al. (2002) to derive the frame moduli. The reason to modify the theory of Chapman et al. (2002) and instead combine it with Gassmann's and Biot's theories is due to the restrictions Chapman et al. (2002) puts on the dry moduli, which are not assumed in Gassmann's or Biot's models. In the theory of Chapman et al. (2002), the dry moduli are functions of the mineral moduli, K_m and μ_m, the stiff and compliant porosity, ϕ_p and ϕ_c, together with the aspect ratio r of the compliant pores. When I use these explicit expressions to model the dry moduli of Westerley Granite and Navajo Sandstone as a function of effective stress for three different aspect ratios and compare them with data of Coyner (1977) taken from Mavko and Jizba (1991) (Figures 2.1 and 2.2), I find a discrepancy between theory and data. No matter the aspect ratios, the model predictions never match the dry data measurements, which in turn would result in inaccurate dispersion estimates for the saturated data. This motivates me to modify the theory where I do not have any restrictions on the dry moduli, in order to use measured dry-rock data as inputs when I model saturated-rock data.

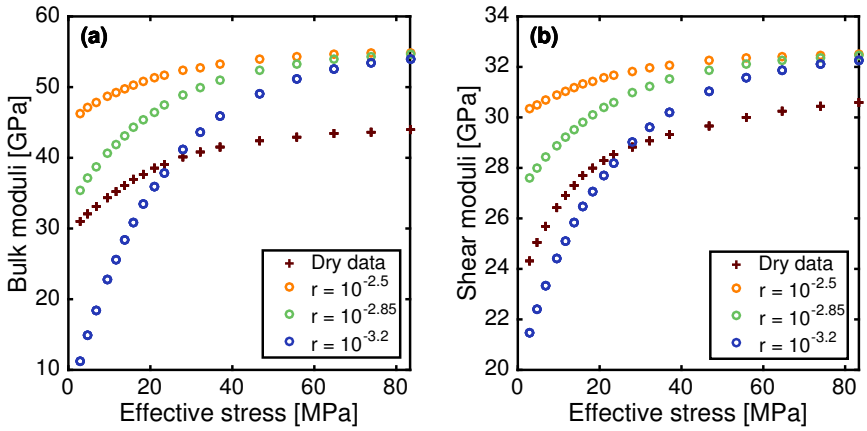

Figure 2.1: Dry bulk (a) and shear (b) moduli as a function of effective stress for Westerley Granite ultrasonic data measurements (red crosses) received from Coyner (1977) but taken from Mavko and Jizba (1991), versus calculated dry moduli using the theory of Chapman et al. (2002). The inputs into the model predictions are the mineral moduli, $K_m = 56$GPa (Mavko and Jizba, 1991) and $\mu_m = 33$GPa (Thompson et al., 2009) and the stiff and compliant pores as a function of effective stress given in Mavko and Jizba (1991). The orange, green and blue circles correspond to aspect ratios, $r = \{10^{-2.5}, 10^{-2.85}, 10^{-3.2}\}$, respectively.

In the first section I review the Chapman et al. (2002) theory and derive frequency-dependent frame moduli for a dry rock containing saturated compliant pores. I then test both the full theory of Chapman et al. (2002) with the newly derived modified frame used in Gassmann (1951) and Biot (1956a), against the theory of Gurevich et al. (2010) and Mavko and Jizba (1991). I do this first for a synthetic fluid-filled rock example as a function of frequency and second for experimental ultrasonic velocity data as a function of effective stress.

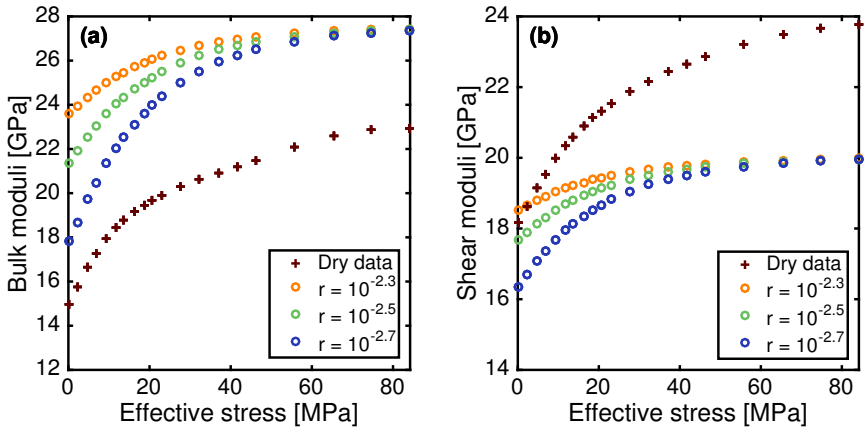

Figure 2.2: Same as Figure 2.1 but for Navajo Sandstone. The inputs to the dry moduli of Chapman et al. (2002) are the bulk and shear mineral moduli, $K_m = 36$GPa (Mavko and Jizba, 1991) and $\mu_m = 26$GPa (Ogushwitz, 1985), with aspect ratios $r = \{10^{-2.3}, 10^{-2.5}, 10^{-2.7}\}$ corresponding to orange, green and blue circles, respectively.

2.3 Theory

2.3.1 Squirt-flow frame moduli

In the following section I review the Chapman et al. (2002) theory and modify it to be combined with Gassmann's and Biot's theories. The theory of Chapman et al. (2002) considered the pore space of the rock to consist of spherical pores and compliant microcracks with small aspect ratios. To calculate the effective bulk and shear moduli, K_{eff} and μ_{eff}, for a small concentration of inclusions, Chapman used the Eshelby (1957) interaction energy approach, which gives the formulas,

$$K_{eff} = K_m - \frac{K_m^2}{\sigma^2} \sum_t \phi_t (\epsilon_{ij}^t \sigma_{kl}^0 - \sigma_{ij}^t \epsilon_{kl}^0), \tag{2.1}$$

and

$$\mu_{eff} = \mu_m - \frac{\mu_m^2}{\sigma^2} \sum_t \phi_t (\epsilon_{ij}^t \sigma_{kl}^0 - \sigma_{ij}^t \epsilon_{kl}^0), \tag{2.2}$$

for the effective bulk and shear moduli. In Equations 2.1 and 2.2, K_m and μ_m refer to mineral bulk and shear moduli, respectively, σ to the the external stress applied, ϕ_t to the different amount of fractional porosities, ϵ_{kl}^0 and σ_{kl}^0 denote the the strains and stresses in the matrix and ϵ_{ij}^t and σ_{ij}^t denote the strains and stresses in the different pore spaces. To find the expressions for the dry effective moduli I set $\sigma_{ij}^t = 0$. The result for the dual system containing stiff spherical pores and compliant ellipsoidal cracks with small aspect ratios following Chapman et al. (2002) and Chapman (2003) is,

$$K_{dry} = K_m - K_m^2 \left(\frac{9(1-\nu)}{4\mu_m(1+\nu)}\phi_p + \frac{\phi_c}{\sigma_c}\right), \tag{2.3}$$

and

$$\mu_{dry} = \mu_m - \mu_m \left(\frac{15(1-\nu)}{(7-5\nu)}\phi_p + \left(\frac{4\mu_m}{15\sigma_c} + \frac{8(1-\nu)}{5(2-\nu)\pi r}\right)\phi_c \right). \tag{2.4}$$

In Equations 2.3 and 2.4, ϕ_p and ϕ_c are the fractional amounts of stiff and compliant pores, the parameter $\sigma_c = \pi\mu_m r/(2(1-\nu))$, with r being the aspect ratio of the microcracks, and ν is the Poisson's ratio of the mineral matrix.

For the expressions of the modified frequency-dependent moduli containing dry stiff pores and fluid-saturated compliant pores, I set $\sigma_{ij}^c = P_c(\omega)$ and $\sigma_{ij}^t = 0$ for all other t, where $P_c(\omega)$ refers to the frequency-dependent fluid pressure in the microcracks. The expressions for the bulk and shear moduli containing microcracks with a normal having Euler angles (θ, ψ) are,

$$K_b(\omega) = K_{dry} + \phi_c \left(\frac{K_m^2}{\sigma_c} + K_m\right)\frac{P_c(\omega)}{\sigma}, \tag{2.5}$$

and

$$\mu_b(\omega) = \mu_{dry} + \phi_c \frac{2\mu_m^2 \sin(\psi)\cos(\psi)\cos(\theta)}{\sigma_c} \frac{P_c(\omega)}{\sigma}. \tag{2.6}$$

The fluid pressure in the compliant pores, P_c, can be found using the equations of Chapman et al. (2002) transformed into the frequency domain,

$$i\omega(m_c - m_p) = \frac{6\rho_f k\zeta}{\eta}(P_p - P_c), \tag{2.7}$$

$$m_c = \frac{\rho_f c_v}{\sigma_c}((1 + K_c)P_c - \sigma_i), \tag{2.8}$$

$$m_p = \frac{3\rho_f p_v}{4\mu_m}((1 + K_p)P_p - \frac{1-\nu}{1+\nu}\sigma_{ii}), \tag{2.9}$$

together with mass balance between the pores,

$$N_c m_c + N_p m_p = 0. \tag{2.10}$$

In Equations 2.7-2.10, m_p and m_c are the masses of the fluids in the stiff round pores and microcracks, respectively, ρ_f is the fluid density, k is the permeability of the rock, ζ is the grain size, η denotes the viscosity of the fluid and P_p is the fluid pressure in the stiff pores. In Equations 2.8 and 2.9, p_v and c_v are the stiff pore and crack volume and $K_p = 4\mu_m/3K_f$, $K_c = \sigma_c/K_f$, where K_f refers to the fluid bulk modulus, σ_i is the normal component of the stress acting on the crack face, σ_{ii} is the trace of the applied stress tensor, and N_c and N_p are the numbers of microcracks and stiff pores in the rock volume. I can solve for the pressure in the form

$$P_c(\omega) = C_1(\omega)\sigma_i + C_2(\omega)\sigma_{ii}, \tag{2.11}$$

where the coefficients $C_1(\omega)$ and $C_2(\omega)$ can be found in Appendix A.

Using Equation 2.11 in Equations 2.5 and 2.6 and assuming a uniform distribution of normal crack directions, I integrate over the Euler angles to find,

$$K_b(\omega) = \text{Real}(K_{dry} + \phi_c(\frac{K_m^2}{\sigma_c} + K_m)(C_1(\omega) + 3C_2(\omega))), \tag{2.12}$$

and

$$\mu_b(\omega) = \text{Real}(\mu_{dry} + \phi_c \frac{4\mu_m^2 C_1(\omega)}{15\sigma_c}), \tag{2.13}$$

for the frequency-dependent dry-rock bulk and shear moduli containing saturated compliant microcracks. Assuming that I do not know the specific pore geometry, I will refer to K_{dry} and μ_{dry} throughout the paper as the dry-frame moduli without explicit expressions. This enables me to use any dry-rock moduli, without having the details of the pore space, when combined with Gassmann's or Biot's theories.

2.4 Squirt-flow model comparison

In this section, I first compare the full Chapman et al. (2002) theory (Equation A.9 and A.10) with Gassmann (1951), Mavko and Jizba (1991) and Gurevich et al. (2010) models. Then I compare the full theory of Chapman with Gassmann's predictions when using the modified frame moduli (Equations 2.12 and 2.13) exchanged as the dry-frame moduli.

The expressions for Mavko and Jizba (1991) high-frequency modified bulk and shear frame moduli, where only compliant pores are fluid filled while

stiffer pores are empty, are given by

$$\frac{1}{K_b} \approx \frac{1}{K_h} + \phi_c(\frac{1}{K_f} - \frac{1}{K_m}) \tag{2.14}$$

and

$$\frac{1}{\mu_b} \approx \frac{1}{\mu_{dry}} - \frac{4}{15}(\frac{1}{K_{dry}} - \frac{1}{K_b}). \tag{2.15}$$

In the Gurevich et al. (2010) theory, the expression for the modified bulk modulus is

$$\frac{1}{K_b(\omega)} = \frac{1}{K_h} + \frac{1}{\frac{1}{\frac{1}{K_{dry}} - \frac{1}{K_h}} + \frac{1}{\phi_c(\frac{1}{K_f^*(\omega)} - \frac{1}{K_m})}}, \tag{2.16}$$

whereas the shear modulus is the same as that of Mavko and Jizba (Equation 2.15) exchanging K_b with $K_b(\omega)$ in Equation 2.16. In both Equations 2.14 and 2.16, K_h refers to the bulk modulus of a hypothetical rock without the compliant pores. The frequency dependence of the modified frame in Equation 2.16 comes from the parameter $K_f^*(\omega)$, which is referred to as the modified fluid bulk modulus derived using the theory of Murphy et al. (1986), given by the expression

$$K_f^*(\omega) = (1 - \frac{2J_1(\hat{k}a)}{\hat{k}aJ_0(\hat{k}a)})K_f, \tag{2.17}$$

where

$$\hat{k}a = \frac{1}{r}\sqrt{-\frac{3i\omega\eta}{K_f}}. \tag{2.18}$$

In Equations 2.17, J_0 and J_1 are the Bessel functions of the first kind and zero and first order, respectively.

The results for the dispersion of a water-saturated rock containing stiff and compliant pores with values given in Tables 2.1 and 2.2 for Gassmann's,

the full theory of Chapman, Mavko-Jizba's and Gurevich et al. theory are shown in Figure 2.3. For these predictions I use Equations 2.3 and 2.4 to calculate the dry moduli and K_h, which contains only the stiff portions of the pores as calculated by setting $\phi_c = 0$ in Equation 2.3. In Figure 2.3, Gassmann's, Mavko-Jizba's, Gurevich et al. and Chapman's bulk and shear moduli as a function of frequency are given by red, orange, purple and blue-green dots, respectively. The time-scale parameter τ, which is a parameter used by the theory of Chapman to adjust at which frequencies the squirt-flow is present, is adjusted to fit with Gurevich et al. model. However, it does not affect the limits of the low- or high-frequency moduli predictions. Another parameter used in Chapman's theory, which is not used in the three other theories, is the shear mineral modulus, μ_m, making up the rock. This physical parameter has negligible effect on the bulk modulus prediction, but it has a significant impact on the effective high-frequency limit of the shear modulus of Chapman et al. (2002). I have chosen the value, μ_m, that makes the high-frequency modulus similar to Mavko-Jizba in Figure 2.3b. My results show that the bulk modulus of Chapman is equivalent to the low-frequncy limit of Gassmann and very close to the high-frequency prediction of Mavko-Jizba, whereas the shear modulus of Chapman can take on multiple high-frequency values as I change μ_m, when I use the dry moduli of Chapman's theory (Equations 2.3 and 2.4).

However, the requirement of using the explicit expressions for the dry moduli, is limiting for the theory considering that a rock that contains the same

amount of porosity and mineral moduli can have different moduli depending on the pore-space structure, while Equations 2.3-2.4 results in only one possible dry bulk and shear moduli value. Furthermore, in Chapman's theory, the stiff pore space is considered perfectly spherical, which if removed allows for a lot more flexibility in the predictive power of the theory. Also, the Eshelby (1957) interaction energy approach (Equations 2.1 and 2.2) is derived assuming a small concentration of pores, which might be violated for high porosity rocks.

I attempt to solve this problem by using the modified frame moduli (Equations 2.12 and 2.13) directly in Gassmann (1951) or Biot (1956a) theories, with no requirements put on the dry moduli, to predict dispersion due to squirt flow or squirt and Biot flow. The comparison between Gassmann, Chapman et al. (2002) full expressions (Equations A.9 and A.10) and the combined Chapman-Gassmann's model is presented in Figure 2.4, red, blue-green dots and purple dashed lines, respectively. In Figure 2.4 I use the same input parameters as in Figure 2.3 and Tables 2.1 and 2.2, with the dry moduli again calculated from Equations 2.3 and 2.4. I find that the combined model somewhat over predicts the low-frequency bulk modulus, Figure 2.4a, while following the full theory of Chapman et al. (2002) in the high frequency regime. However, I have no restrictions set on how to choose my dry moduli when using the combined model. The shear modulus follows the full theory well for all frequencies. I learn from the results that for Chapman et al. (2002) theory, it is a correct assumption to state that the high-frequency modified dry moduli to be used in Gassmann (1951) theory to add the effect of squirt-flow

Table 2.1: Parameters used to compare Chapman et al. (2002) theory with Gassmann (1951), Mavko and Jizba (1991) and Gurevich et al. (2010) models. The terms K_m and μ_m are the mineral grains bulk and shear moduli, ϕ_s and ϵ are the stiff porosity and the crack density, related to the compliant porosity ϕ_c and aspect ratio r as $\epsilon = 3\phi_c/(4\pi r)$. The timescale parameter in Chapman's theory is represented by τ.

K_m [GPa]	μ_m [GPa]	ϕ_s [%]
35	27	20
ϵ [−]	r [−]	τ [s]
0.02	10^{-3}	$10^{-4.9}$

Table 2.2: Parameters used for the saturating fluid, being water, K_f and ρ_f refers to the fluid moduli and density, and η is the viscosity. Values come from Coyner (1977).

K_f [GPa]	ρ_f [kg/m^3]	η [Pa $\cdot$ s]
2.24	10^3	10^{-3}

consists of the dry rock with saturated compliant microcracks.

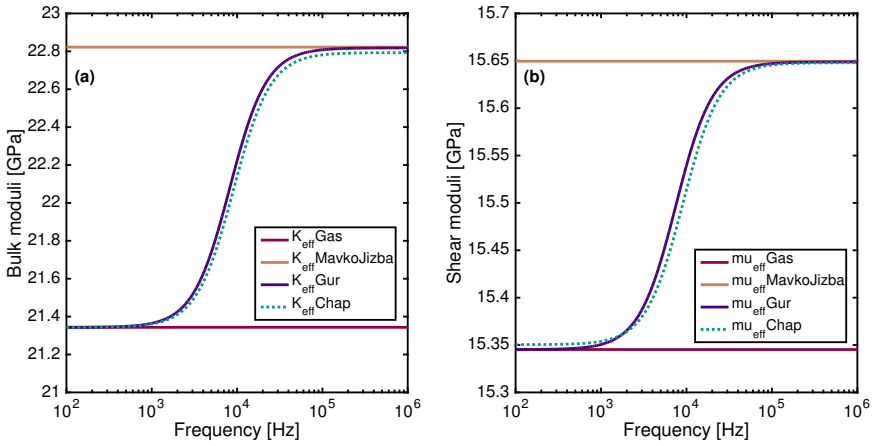

Figure 2.3: Calculated bulk (a) and shear (b) moduli dispersion for a sandstone saturated with water (Tables 2.1-2.2) using the theory of Gassmann (1951) (red), Mavko and Jizba (1991) (orange), Gurevich et al. (2010) (purple) and the full theory of Chapman et al. (2002) (blue-green dots). The dry bulk and shear moduli are given by Equation 2.3 and 2.4, while K_h, which contains only the stiff pores used by the Mavko-Jizba's and the Gurevich et al. theory is calculated using the theory of Chapman, Equation 2.3 setting $\phi_c = 0$. The bulk moduli for Chapman is seen to be consistent with Gassmann in the low and very close to the Mavko-Jizba theory in the high-frequency regime, whereas Chapman's shear moduli can take on multiple upper limit values as I change μ_m, a parameter not used in the three other theories. I have adjusted μ_m so that the upper high-frequency limit is close to Mavko-Jizba's result, while I set the time-scale parameter τ, so that the frequency dependence of Chapman's model is similar to Gurevich et al. model.

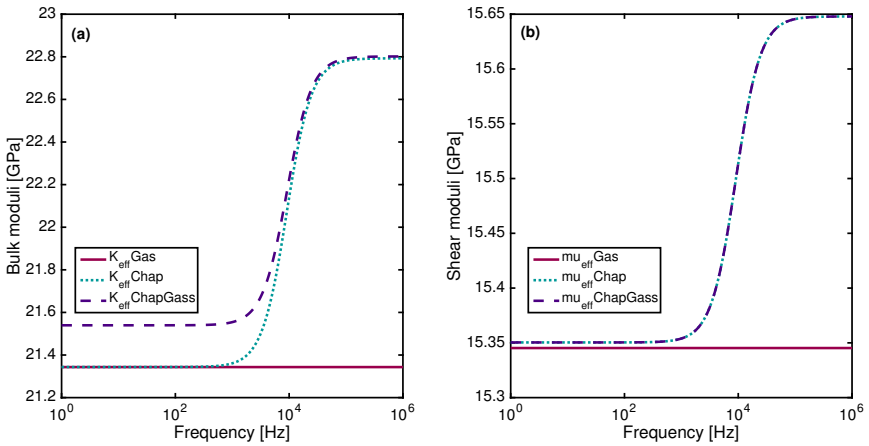

Figure 2.4: Bulk (a) and shear (b) moduli dispersion for a sandstone saturated with water (Tables 2.1-2.2) using the theory of Gassmann (red), full theory of Chapman (blue-green) and combined Chapman-Gassmann model (purple). I use $K_{dry} \approx 19$GPa and $\mu_{dry} \approx 15$GPa calculated from Equations 2.3 and 2.4. Chapman's bulk moduli (a) agrees well with Gassmann's moduli in the low-frequency regime, while the combined Chapman-Gassmann model somewhat over predicts the value. However, Chapman's and the combined Chapman-Gassmann model is seen to predict the same high-frequency limit.

In Figure 2.5 I change the dry moduli to be $K_{dry} = 16$GPa and $\mu_{dry} = 14$GPa, which are different from the values received from Equations 2.3 and 2.4, while keeping all other parameters the same. I now find a discrepancy between Chapman et al. (2002) and Gassmann (1951) bulk moduli in the low-frequency regime (Figure 2.5a). The combined model, however, which still somewhat over predicts the low-frequency bulk modulus, should still provide a good high-frequency squirt-flow prediction based on previous results (Figure 2.4a). The shear modulus for both the full and combined theories, Figure 2.5b, are consistent with Gassmann in the low-frequency regime and follow

each other for the high frequencies.

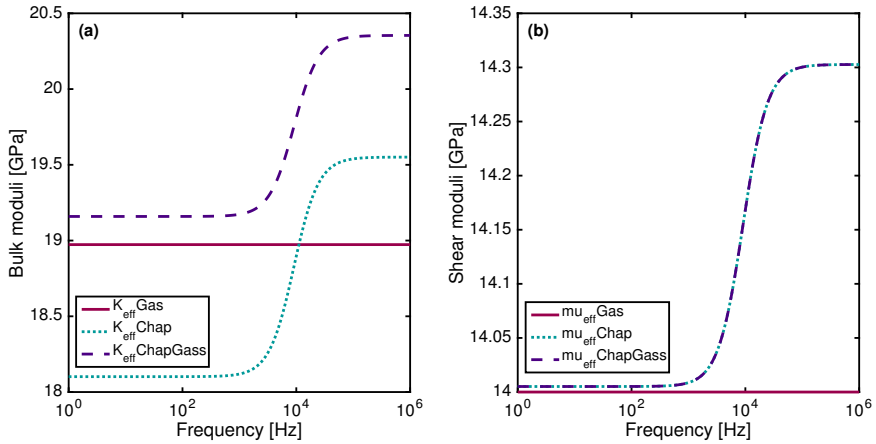

Figure 2.5: Same as Figure 2.4, but instead of using explicit expressions for the dry modulus I set them to be $K_{dry} = 16$GPa and $\mu_{dry} = 14$GPa.

For a better understanding of the different models I summarize the parameters that are needed for the the three modified dry-frame moduli combined with Gassmann's theory to predict squirt flow dispersion in Table 2.3 for Chapman's, Equations 2.12 and 2.13, Gurevich et al. (2010), Equations 2.16 and 2.15, and Mavko and Jizba (1991), Equations 2.14 and 2.15. I find the two main parameters that differentiates my modified Chapman's theory from Mavko-Jizba's and Gurevich et al. theories to be μ_m and K_h.

2.5 Comparing models to data

I use ultrasonic laboratory measurements for both the compressional, P, and shear, S, wave velocities as a function of effective stress from the work of Coyner (1977) presented in Mavko and Jizba (1991) for Westerley Granite

Table 2.3: Parameters used in the modified frame moduli derived from Chapman et al. (2002), with the theories of Gurevich et al. (2010) and Mavko and Jizba (1991) squirt flow theories combined with Gassmann (1951) referred to as C, G and MJ in the table.

Parameters	Definitions	C	G	MJ
K_{dry}	Dry bulk moduli	✓	✓	✓
K_h	Dry bulk moduli without compliant pores	✗	✓	✓
μ_{dry}	Dry shear moduli	✓	✓	✓
K_m	Mineral bulk moduli	✓	✓	✓
μ_m	Mineral shear moduli	✓	✗	✗
ϕ_c	Compliant porosity	✓	✓	✓
ϕ	Total porosity	✓	✓	✓
r	Aspect ratio of compliant pores	✓	✓	✗
τ	Timescale parameter	✓	✗	✗
K_f	Fluid bulk moduli	✓	✓	✓
η	Fluid viscosity	✓	✓	✗

and Navajo Sandstone to test the different theories. The inputs to the models received from laboratory measurements are the dry P- and S-wave velocities, along with total porosity and compliant porosity as a function of effective stress. The other parameters used to test the model predictions on the two rock samples are given in Tables 2.4 and 2.5, and the values for the saturating fluid are presented in Table 2.2. All the parameters in the tables are assumed to be constant with respect to effective stress. The values for the mineral bulk moduli and densities for both rocks are taken from Mavko and Jizba (1991), whereas the shear mineral moduli and permeabilities for Westerley Granite and Navajo Sandstone are given in Thompson et al. (2009); Zhang (2013) and Ogushwitz (1985). The chosen permeabilities ensure that I am in the high-frequency regime for the Biot dispersion. The values for the timescale

Table 2.4: Parameters used in the different models for Westerley Granite. K_m, μ_m, and ρ_m refers to the bulk modulus, shear modulus and density of the mineral, k is the permeability, r is the aspect ratio of the cracks and τ is the timescale parameter for Chapman's squirt flow model.

K_m [GPa]	μ_m [GPa]	ρ_m [kg/m^3]
56	33	$2.64{\cdot}10^3$
k [D]	r [-]	τ [s]
10^{-7}	$10^{-2.85}$	$4{\cdot}10^{-3}$

parameters are estimated using Equation A.7, whereas the aspect ratios are used as fitting parameters with optimal values for each rock type given in Tables 2.4-2.5. I compare the measured ultrasonic velocity data for the saturated rocks against Gassmann (1951), Biot (1956a), my modified Chapman's and Mavko and Jizba (1991) frame moduli, Equations 2.12, 2.13, 2.14 and 2.15, combined with Biot's theory in Appendix B. I do not use the Gurevich et al. (2010) model because it predicts the same high-frequency moduli as the Mavko and Jizba (1991) theory. I set the tortuosity $\alpha = 1.25$ in Biot's theory for both rock types, similar to what was done by Stoll (1977) to model sands. The results for the different model predictions together with the data are given in Figures 2.6 and 2.7. Red and blue crosses correspond to the dry and water-saturated laboratory measurements. The light-blue region represents the area which is within 2% and 3% error for the P- and S-wave saturated velocity data, respectively. The different predictions of Gassmann, Biot, Mavko-Jizba and my combined Biot-Chapman models are given by purple squares, gray crosses, pink crosses and green circles, respectively.

I find the predictions from the Biot-Chapman model to be in rather

Table 2.5: Parameters used in the different models for Navajo Sandstone similar to Table 2.4

K_m [GPa]	μ_m [GPa]	ρ_m [kg/m^3]
36	26	$2.63{\cdot}10^3$
k [D]	r [-]	τ [s]
0.1	$10^{-2.5}$	$4{\cdot}10^{-6}$

good correspondence to the saturated P-wave velocity data for Westerley Granite (Figure 2.6a) whereas the S-wave model predictions are seen to be a bit too low (Figure 2.6b). The Mavko-Jizba predictions follow Biot-Chapman closely, with the latter being a bit closer to the data. I also conclude the Biot dispersion to be negligible for Westerley Granite considering it is almost the same as the Gassmann's predictions. I observe both the Biot-Chapman and the Mavko-Jizba models to converge to the Biot predictions with increasing effective stress, due to the closing of compliant pores.

The results for Navajo Sandstone can be seen in Figure 2.7. I find the Biot-Chapman's predictions and the measured saturated P-wave velocities to be close to one another for low and high effective stresses, whereas Mavko-Jizba's model somewhat over-predicts the P-wave velocities for lower stresses. For the S-wave velocity predictions the Biot-Chapman under-predicts the velocities, while Mavko-Jizba over-predicts them. However, both Biot-Chapman and Mavko-Jizba models converge to one another with increasing effective stress. I also find Biot dispersion to be higher in Navajo Sandstone than in Westerley Granite due to an increase in total porosity. For both the P- and S-wave velocities, I notice the slope of the dispersion for the saturated data to

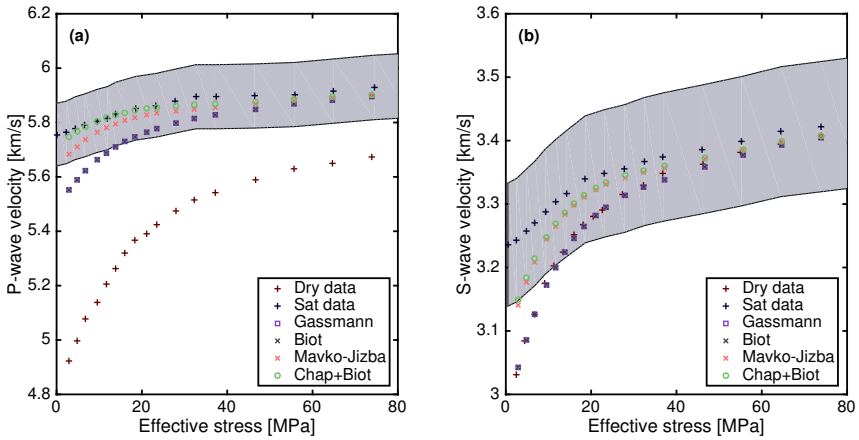

Figure 2.6: Comparison between Westerley Granite ultrasonic laboratory measurements from (Coyner, 1977; Mavko and Jizba, 1991) and model predictions as a function of effective stress. Red and blue crosses correspond to dry and water saturated data, and the light-gray region is within 2% and 3% error for the P-wave (a) and S-wave saturated velocities (b). Purple squares, gray crosses, pink crosses and green circles are the predictions of Gassmann, Biot, Mavko-Jizba and my combined Biot-Chapman model, respectively.

be higher for lower pressures compared to either Biot-Chapman's or Mavko-Jizba's predictions. An explanation for this could be the decrease in estimated aspect ratios as a function of effective stress since this would increase the velocities further. However, I decided not to pursue this question in this study.

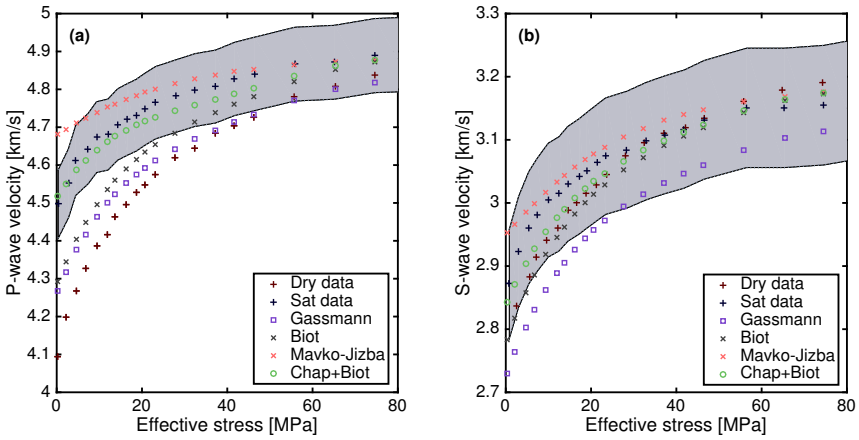

Figure 2.7: Ultrasonic laboratory data for dry (red crosses) and saturated (blue crosses) Navajo sandstone (Coyner, 1977; Mavko and Jizba, 1991). The predicted velocities for Gassmann, Biot, Mavko-Jizba and my combined Biot-Chapman model, respectively, are given by purple squares, gray crosses, pink crosses and green circles. The gray shaded region represents 2% and 3% error for the P-wave (a) and S-wave saturated velocities (b).

2.6 Conclusions

I have demonstrated how to derive a modified dry-frame moduli containing fluid-saturated compliant pores using Chapman's squirt-flow formalism. These frame moduli can be incorporated into Gassmann's or Biot's theory to estimate either squirt flow or the combined dispersion effect from Biot and squirt flow over all frequencies. Even though the combined theory somewhat over predicts the bulk moduli for the low-frequency regime it does not put any restrictions on the dry moduli, and it is equivalent to the high-frequency limit of Chapman's full theory when incorporated into Gassmann's model. I also find the full theory of Chapman and the Gurevich et al. (2010) model to predict similar bulk-moduli dispersion when using the explicit expressions for the dry moduli given explicitly by Chapman's theory, where the low- and high-frequency limits are given by Gassmann's and Mavko-Jizba's models. The shear modulus for Chapman's theory on the other hand can take on multiple upper-limit values as a function of the shear mineral moduli, not used in Gurevich et al. or Mavko-Jizba's theory. When I test my combined theory of Biot-Chapman, using the dry measured velocities, against ultrasonic saturated velocity measurements, I find the theory to perform a little bit better then Mavko-Jizba's predictions. I believe the reason might be due to the difficulty in predicting correct values for the dry moduli without compliant pores, which is used in both Gurevich et al. and Mavko-Jizba's theories.

Chapter 3

Local and global fluid effects on sonic wave modes

3.1 Abstract

[1] Most subsurface formations of value to exploration contain heterogeneous fluid-filled pore space, where local fluid-pressure effects can significantly change the velocities of passing seismic waves. To understand better the effect of these local pressure gradients on borehole wave propagation, I combined Chapman's squirt-flow model with Biot's poroelastic theory. I applied the unified theory to a slow and fast formation with permeable borehole walls containing different quantities of compliant pores. These results were compared to those for a formation with no soft pores. The discrete wavenumber summation method with a monopole point source generated the wavefields consisting of five different receiver wave modes, the P-, S-, leaky-P, Stoneley and pseudo-Rayleigh waves. I neglected the effects of a borehole tool in order to isolate the wave-induced fluid effects. The resulting synthetic wave modes were pro-

[1]Parts of this chapter was first published in Dahl, E.J.H. and K.T.Spikes, "Dispersion in sonic wave modes caused by global and local flow", SEG expanded abstracts, 2016. The peer-reviewed version of this paper can be found in Dahl, E.J.H. and K.T.Spikes. "Local and global fluid effects on sonic wave modes". Geophysics, 82:1-13, 2017. For these two papers I provided all the technical work and wrote the two manuscripts, Kyle reviewed and helped in the revisions process.

cessed using a weighted spectral semblance (WSS) algorithm. I found that the resulting WSS dispersion curves closely match the analytical expressions for the formation compressional velocity and solutions to the period equation for dispersion for the P-wave, Stoneley and pseudo-Rayleigh wave phase velocities in both slow and fast formations. The WSS applied to the S-wave part of the waveforms, however, did not correlate as well with its respective analytical expression for formation shear wave velocity, most likely due to interference of the pseudo-Rayleigh wave. To separate changes in formation compressional- and shear-wave velocities versus fluid flow effects on the Stoneley-wave mode, I computed the slow-P wave dispersion for the same formations. I found that fluid-saturated soft pores significantly affected both the P- and S-wave effective formation velocities, whereas the slow-P wave velocity was rather insensitive to the compliant pores. Thus, the large phase-velocity effect on the Stoneley wave mode was mainly due to changes in effective formation P- and S-wave velocities and not to additional fluid mobility.

3.2 Introduction

Borehole acoustic logging is an extremely valuable tool for petroleum reservoir exploration, hydrocarbon production, reserve estimation and well completions (Tang and Cheng, 2004). Numerical modeling has been the main approach to study full waveforms in boreholes. Common methods are, e.g., quasi-analytical, finite-difference and finite-element modeling. Usually quasi-analytical methods assume axial symmetry and are not applicable to forma-

tions varying in the vertical direction (i.e., layering). These 1D methods have been useful to analyze the waveforms and dispersion of different wave modes in isotropic formations (Tsang and Rader, 1979; Cheng and Toksöz, 1981; Tang and Cheng, 2004), isotropic formations with radial layers (Schmitt, 1988b) and transversely-isotropic formations (White and Tongtaow, 1981; Tang and Cheng, 2004). The formations of economic interest in exploration usually contain mobile fluids, which are considered to be the main contributors to seismic attenuation and dispersion (Mavko et al., 2009). Four major fluid-dispersion mechanisms have been recognized. They are Biot flow, squirt flow, patchy saturation and viscous shear. Squirt flow appears to be important in the sonic-frequency regime (Chotiros and Isakson, 2004; Sun et al., 2016). In this paper I focus on the first two mechanisms, Biot and squirt flow.

Biot (1956a,b) theory attempts to explain wave propagation resulting from wave-induced fluid flow (WIFF) due to wavelength-scale pressure differences in porous saturated media, where the fluid is coupled with the solid movement through viscous and inertial forces. Biot's WIFF is often referred to as global or macroscopic flow due to the details of pore shape and local flow not being considered. These properties are instead included in parameters averaged on a scale much larger than the pore size. In Biot's theory, three types of waves can propagate in the fluid-saturated poroelastic medium. They are the fast P-wave, the S-wave and the slow-P wave. The fast P-wave and the S-wave are mostly affected by the solid formation velocities, whereas the slow-P wave is primarily affected by the motion in the pore fluid. Several theoretical studies

on sonic waveforms include Biot's theory of poroelasticity (e.g., Rosenbaum, 1974; Schmitt, 1988a; Tang and Cheng, 2004), which show that the Stoneley wave is sensitive to the in situ mobility of the saturated porous formation whereas the P- and S-wave modes are not. However, Dvorkin et al. (1994) and Dvorkin and Nur (1993) found that Biot's theory alone cannot explain the P-wave attenuation and dispersion observed in many different sandstone measurements. A combined Biot-squirt flow theory, referred to as BISQ (Biot squirt flow), provided a fit to the laboratory data. Unfortunately, BISQ theory does not agree with Gassmann's prediction in the low-frequency limit (Mavko et al., 2009). Both Biot and squirt-flow models have separately been able to explain observed P-wave dispersion in well log data (e.g., Baron and Holliger, 2010; Sun et al., 2016).

Pressure differences in pore-space heterogeneity cause squirt flow (Mavko and Nur, 1975). Some theoretical squirt-flow models focus on aspect-ratio distributions (O'Connell and Budiansky, 1977; Palmer and Traviola, 1980), whereas others assume the pore space to have a binary structure of stiff and compliant pores (Shapiro, 2003; Chapman et al., 2002; Gurevich et al., 2010). Biot's theory has also been utilized to derive the response of a dual-porosity medium to investigate the effect of heterogeneity in the pore space (Pride and Berryman, 2003a,b). The approach taken in this paper is to combine Biot's poroelastic theory with a frequency-dependent rock frame from Chapman et al. (2002). Previously, Keller (1989) used the constant-Q composite model to derive a frequency-dependent modulus, which was included in Biot

(1957) theory for isotropic saturated media. With this model Keller obtained a good match between experimentally measured and modeled P-wave attenuation. A similar study to ours is that of Markova et al. (2014) who used Gurevich et al. (2010) theory to investigate the effect of squirt flow on acoustic waveforms. My study differs from previous work in both the unification of global and local flow and that I analyze the dispersion of the computed P-, S-, Stoneley and pseudo-Rayleigh waves. This dispersion is studied using both weighted spectral semblance (WSS) (Nolte and Huang, 1997) and analytical expressions.

The objective of this study is to analyze the effect that Biot and squirt flow have on borehole acoustic monopole wave modes with an emphasis on squirt flow. This is considered an ideal study where I neglect the effects of the tool response, borehole rugosity, mud cake, dipping layers and anisotropy. I am aware that these parameters influence the wave modes to different degrees and might make this study less practical. However, it is still of importance to understand the isolated effect that fluid-saturated compliant pores have on wave propagation in boreholes. I study two formations, a slow and a fast, by simulating waveforms using the discrete wavenumber summation method. The analytical dispersion is then compared to the waveform processed WSS dispersion.

3.3 Theory

3.3.1 Poroelastic wave equation with frequency-dependent coefficients

In my approach of incorporating squirt flow into Biot's poroelastic theory, I consider a dual system of porosity. The void space consists of evenly distributed compliant microcracks with small aspect ratios and uniformly sized stiffer pores. The pore space is all interconnected. I assume the rock to be statistically isotropic on a macroscopic scale, allowing me to use the equation of motion in a poroelastic medium described by Biot (1956a),

$$(A+\mu)\nabla\nabla\cdot\mathbf{u}+\mu\nabla^2\mathbf{u}+Q\nabla\nabla\cdot\mathbf{U}=\rho_{11}\ddot{\mathbf{u}}+\rho_{12}\ddot{\mathbf{U}}+b(\dot{\mathbf{u}}-\dot{\mathbf{U}}), \tag{3.1}$$

$$Q\nabla\nabla\cdot\mathbf{u}+R\nabla\nabla\cdot\mathbf{U}=\rho_{12}\ddot{\mathbf{u}}+\rho_{22}\ddot{\mathbf{U}}-b(\dot{\mathbf{u}}-\dot{\mathbf{U}}), \tag{3.2}$$

where $\mathbf{u}$ and $\mathbf{U}$ are the average displacement vectors in the solid and the fluid phase, respectively. The coefficients are $\rho_{11}=(1-\phi)\rho_m-(1-\alpha)\phi\rho_f$, $\rho_{22}=\alpha\phi\rho_f$ and $\rho_{12}=(1-\alpha)\phi\rho_f$ (Plona and Johnson, 1980; Mavko et al., 2009), where ρ_m and ρ_f are the densities of the mineral and the fluid, respectively, and ϕ denotes the porosity. Above, α is the tortuosity, a purely geometric factor that describes the fluid connectivity of the pore space. It gives a measure of the average ratio between fluid path length and displacement.

The coefficient b is related to permeability k and fluid viscosity η by $b=\eta\phi^2/k$ (Biot, 1956a). The theory of Biot has previously been extended by Biot (1962a,b) to include viscoelasticity and solid dissipation. The theory was advanced by exchanging the elastic coefficients with operators. The following

derivation motivates why it is accurate to replace the frame moduli with bulk and shear moduli containing saturated compliant and dry stiff pores in order to explain a dual-porosity medium. Biot (1957) performed three ideal thought experiments under static conditions for a single-porosity medium to derive the expressions for the four elastic coefficients A, μ, Q, and R. To derive the four elastic coefficients in a dual system of porosity with compliant and stiff pores, I apply the same three experiments now under high- and low-frequency conditions although using the same stress strain relationship (Biot, 1962a),

$$\sigma_{ij} = 2\mu e_{ij} + \delta_{ij}(Ae_{kk} + Q\epsilon_{kk}), \tag{3.3}$$

$$s = Qe_{kk} + R\epsilon_{kk}. \tag{3.4}$$

The low-frequency regime refers to the frequency below the squirt-flow critical frequency. The high-frequency regime refers to frequencies above the critical frequency (see e.g., Mavko et al., 2009). In equations 3.3 and 3.4 σ_{ij} and s are the stress tensor in the solid phase and tension in the pore fluid phase, respectively, related to pore-fluid pressure by $s = -\phi p$. The strains e_{ij}, e_{kk} and ϵ_{kk} are related to the displacement in the solid and the fluid by $e_{ij} = (u_{i,j} + u_{j,i})/2$, $e_{kk} = \nabla \cdot \mathbf{u}$ and $\epsilon_{kk} = \nabla \cdot \mathbf{U}$. In the first ideal experiment I consider the material to be subjected to pure shear stress. In the low-frequency regime I assume the pore pressures have enough time to equilibrate in the randomly oriented compliant microcracks but not in the high-frequency regime. I express this as

$$\mu = \mu_b(\omega), \tag{3.5}$$

where $\mu_b(\omega)$ is the frequency-dependent shear modulus containing dry microcracks and dry stiff pores in the low-frequency regime and saturated microcracks and dry stiff pores in the high-frequency regime. In the second experiment the rock sample is covered in a flexible, impermeable jacket subjected to a hydrostatic pressure p. The pore pressure inside the jacket is held constant at 1 atm by letting the fluid flow in and out through a tube exposed to the atmosphere (Carcione, 2014). Using equations 3.3 and 3.4 I find

$$-p = \frac{2}{3}\mu e_{kk} + Ae_{kk} + Q\epsilon_{kk} \tag{3.6}$$

and

$$0 = Qe_{kk} + R\epsilon_{kk}. \tag{3.7}$$

For low frequencies, I assume the pressure to be transmitted to the dry frame. For high frequencies, the pressure is instead transmitted to the frame containing saturated compliant microcracks and dry stiff pores expressed as

$$K_b(\omega) = -p/e_{kk}. \tag{3.8}$$

Equations 3.6, 3.7 and 3.8 give

$$\frac{2}{3}\mu + A - \frac{Q^2}{R} = K_b(\omega). \tag{3.9}$$

In the third experiment, which is an unjacketed test, the saturated rock sample is subjected to a hydrostatic pressure p_f. Equations 3.3 and 3.4 give

$$-(1-\phi)p_f = \frac{2}{3}\mu e_{kk} + Ae_{kk} + Q\epsilon_{kk} \tag{3.10}$$

and

$$-\phi p_f = Qe_{kk} + R\epsilon_{kk}. \tag{3.11}$$

I also have the relationships for the bulk modulus of the fluid,

$$K_f = -p_f/\epsilon_{kk}, \tag{3.12}$$

and

$$K_m(\omega) = -p_f/e_{kk}, \tag{3.13}$$

where $K_m(\omega)$ is assumed to be the pure mineral bulk modulus of the rock sample for low frequencies and the bulk modulus of the mineral containing saturated compliant microcracks for high frequencies. Equations 3.10, 3.11, 3.12 and 3.13 give

$$(1-\phi) = \frac{2\mu/3 + A}{K_m(\omega)} + \frac{Q}{K_f} \tag{3.14}$$

and

$$\phi = \frac{Q}{K_m(\omega)} + \frac{R}{K_f}. \tag{3.15}$$

From equations 3.5, 3.9, 3.14 and 3.15 I find the expressions for the frequency-dependent coefficients,

$$A(\omega) = \frac{(1-\phi)(1-\phi-\frac{K_b(\omega)}{K_m(\omega)})K_m(\omega) + \phi\frac{K_m(\omega)}{K_f}K_b(\omega)}{1-\phi-\frac{K_b(\omega)}{K_m(\omega)} + \phi\frac{K_m(\omega)}{K_f}} - \frac{2}{3}\mu_b(\omega), \tag{3.16}$$

$$\mu(\omega) = \mu_b(\omega), \tag{3.17}$$

$$Q(\omega) = \frac{(1-\phi-\frac{K_b(\omega)}{K_m(\omega)})\phi K_m(\omega)}{1-\phi-\frac{K_b(\omega)}{K_m(\omega)} + \phi\frac{K_m(\omega)}{K_f}}, \tag{3.18}$$

$$R(\omega) = \frac{\phi^2 K_m(\omega)}{1-\phi-\frac{K_b(\omega)}{K_m(\omega)} + \phi\frac{K_m(\omega)}{K_f}}. \tag{3.19}$$

I will now use Chapmans squirt flow formalism to provide expressions for $K_b(\omega)$ and $\mu_b(\omega)$, which appear in equations 3.16-3.19.

3.3.2 Squirt-flow moduli

The typical order of magnitude for compliant porosity is approximately $\phi_c = 0.001$ for porous sandstone (Shapiro, 2003). With this in mind I make an assumption to simplify my model. I approximate the low-frequency bulk and shear moduli containing dry compliant and stiff pores to be equal to the low-frequency bulk and shear moduli containing saturated compliant and dry stiff pores. This enables the use of the Chapman et al. (2002) model. I also assume that in the high-frequency regime the bulk moduli of the mineral containing saturated compliant microcracks is approximately equal to the pure mineral moduli, thus $K_m(\omega) = K_m$ in the preceding expressions.

Chapman et al. (2002) derived a squirt-flow model for ellipsoidal microcracks with small aspect ratios and uniformly sized spherical pores. Fluids are free to move between the two different pore spaces. Chapman et al. (2002) used the Eshelby (1957) interaction energy formula to derive an expression for the effective elastic stiffness tensor C^{eff}_{ijkl} as a function of the matrix elastic stiffness tensor C_{ijkl}, the different porosities ϕ_t, the strains and stresses in the matrix ϵ^0_{kl}, σ^0_{kl}, respectively, and in the different pore spaces ϵ^t_{ij}, σ^t_{ij},

$$C^{eff}_{ijkl}\epsilon^0_{ij}\epsilon^0_{kl} = C_{ijkl}\epsilon^0_{ij}\epsilon^0_{kl} - \sum_t \phi_t(\epsilon^t_{ij}\sigma^0_{kl} - \sigma^t_{ij}\epsilon^0_{kl}). \tag{3.20}$$

In the expression above, $\phi_t(\epsilon^t_{ij}\sigma^0_{kl} - \sigma^t_{ij}\epsilon^0_{kl})$ represents the perturbations to the effective elastic stiffness tensor by the different porosity types. Following

Chapman et al. (2002) and Chapman (2003) I find,

$$K_b(\omega) = \mathrm{Re}(K_{dry} + \phi_c(\frac{K_m^2}{\sigma_c} + K_m)(C_1(\omega) + 3C_2(\omega))), \tag{3.21}$$

for the frequency-dependent dry rock bulk modulus containing saturated microcracks. Here K_{dry} is the dry bulk modulus including the dry compliant microcracks. The effect of the compliant porosity on the dry moduli in Chapman et al. (2002) theory is given by,

$$K_{dry} = K^*_{dry} - K_m^2 \frac{\phi_c}{\sigma_c}, \tag{3.22}$$

where K^*_{dry} refers to the dry rock modulus without compliant pores. In equations 3.21 and 3.22 K_m is the mineral modulus, ϕ_c is the crack porosity, and $\sigma_c = \pi\mu_m r/(2(1-\nu))$, r being the aspect ratio of the cracks, and μ_m and ν are the shear modulus and Poisson's ratio of the mineral respectively. The expressions for $C_1(\omega)$ and $C_2(\omega)$ are given in Appendix A.

The effective frequency-dependent dry shear modulus containing saturated microcracks is given by

$$\mu_b(\omega) = \mathrm{Re}(\mu_{dry} + \phi_c \frac{4\mu_m^2 C_1(\omega)}{15\sigma_c}), \tag{3.23}$$

where μ_{dry} is the dry shear modulus, which is affected by the compliant microcracks through the following relationship,

$$\mu_{dry} = \mu^*_{dry} - \mu_m(\frac{4\mu_m}{15\sigma_c} + \frac{8(1-\nu)}{5(2-\nu)\pi r})\phi_c, \tag{3.24}$$

where μ^*_{dry} corresponds to the dry shear modulus without compliant pores.

Equations 3.21 and 3.23 are used in equations 3.16-3.19 to include the effects of squirt flow. Note that when no compliant pores are present, $\phi_c = 0$, Equations 3.21 and 3.23 reduce to K^*_{dry} and μ^*_{dry}, representing only Biot flow.

3.4 Numerical examples

In this section I investigate the effects of a poroelastic formation considering both Biot and squirt-flow dissipation. I use the discrete wavenumber summation method to generate the wavefields (Cheng and Toksöz, 1981; Tang and Cheng, 2004), see Appendix C. The borehole is assumed to be axisymmetric with a permeable interface. The tool has been neglected to study better the dispersion effects on the waveforms.

I analyze the effects of compliant pores in a fast and a slow fluid-saturated formation, similar to the ones presented in (Schmitt, 1988c). Table 3.1 contains the rock-property values for both the slow and the fast formations. The fluid in the borehole and saturating fluid is assumed to be water (see Table 3.2). In the following examples the borehole radius is $R_{bh} = 12$ cm, the source to first receiver distance $z_1 = 5.25$ m, the inter-receiver distance is $\Delta z = 0.1524$ m, and I use 13 receivers. The center frequencies for the two monopole sources are $\omega_0 = 2\pi \cdot 7.5$ kHz and $\omega_0 = 2\pi \cdot 1$ kHz.

3.4.1 Slow formation

In a slow formation, i.e., one where the formation shear velocity is less than the compressional velocity in the borehole fluid, the observed wave modes

Table 3.1: Parameters for porous slow and fast formations containing compliant pores. The terms K_m, μ_m and ρ_m are the mineral grains bulk, shear and density. Here, K^*_{dry} and μ^*_{dry} are the dry porous rock excluding the compliant pores bulk and shear moduli, and ϕ_s, ϵ and ϕ_c are the stiff porosity, the crack density and the compliant porosity, calculated from the crack density. Terms k and α are the permeability and tortuosity respectively. For a random system $\alpha = 3$ (Stoll, 1977). The aspect ratio is r and the timescale parameter τ. An estimate is $\tau \approx 10^{-5}$ s for water-saturated sandstone (Chapman, 2001).

Slow formation					
K_m [GPa]	μ_m [GPa]	ρ_m [kg/m^3]	K^*_{dry} [GPa]	μ^*_{dry} [GPa]	ϕ_s [%]
35	32	2600	5.5	3.8	20
ϵ [−]	ϕ_c [%]	k [D]	α [−]	r [−]	τ [s]
0-0.04	0-0.00168	0.2	3	10^{-4}	10^{-5}
Fast formation					
K_m [GPa]	μ_m [GPa]	ρ_m [kg/m^3]	K^*_{dry} [GPa]	μ^*_{dry} [GPa]	ϕ_s [%]
37.9	32	2650	15.4	10.1	19
ϵ [−]	ϕ_c [%]	k [D]	α [−]	r [−]	τ [s]
0-0.08	0-0.00335	0.2	3	10^{-4}	10^{-5}

Table 3.2: Parameters for the borehole and saturating fluid. The terms K_f, ρ_f and η are the bulk modulus, density and viscosity of the fluid..

K_f [GPa]	ρ_f [kg/m^3]	η [Pa · s]
2.25	10^3	10^{-3}

in the waveforms are the refracted P-wave, the leaky-P and the Stoneley wave (e.g., Tichelaar and van Luik, 1995). The compressional velocity of the formation is the upper bound for the leaky-P wave velocity. This mode loses energy by conversion to shear, which radiates into the formation (Tang and Cheng, 2004). The Stoneley wave is an interface wave between the borehole fluid and the surrounding formation, which exists at all frequencies. It is slightly dispersive and attenuates approximately exponentially away from the borehole wall in an isotropic formation (Cheng and Toksöz, 1981). It dominates the low-frequency part of the waveforms. The dispersion of the Stoneley wave is relatively insensitive to permeability when the borehole wall is impermeable. When the borehole wall is permeable, the phase velocity decreases as permeability increases (Schmitt, 1988c). The permeability estimation is best demonstrated with a low-frequency source ($\leq$ 3 kHz). The effect of permeability on borehole acoustic waves is mainly through the excitation and propagation of the slow-P wave (Tang and Cheng, 2004). This is why Tang et al. (1991) could successfully decompose the Stoneley wave borehole interaction into two parts. The first is due to the formation P- and S-wave interaction in absence of the slow-P wave and secondly due to the formation slow-P wave.

Figure 3.1 shows the effective fast P- and S-wave formation velocity dispersion using Equations C.6, C.7 and the relationship $V(\omega) = \omega/k(\omega)$ for three different crack densities $\epsilon = 0, 0.02$ and 0.04. The crack porosity is related to crack density by $\phi_c = 4\pi\epsilon r/3$, giving the porosities $\phi_c = 0, 0.00084$ and 0.00168%. Black lines, corresponding to no compliant pores, show little

to no dispersion. Biot flow causes this dispersion. With a small addition of compliant pores, red and blue lines, I observe a decrease in velocities at low frequencies and a significant increase in dispersion for both the P- and the S-wave. The P-wave velocity dispersion for the formation with crack density of $\epsilon = 0.04$ is almost 250 m/s and around 150 m/s for the S-wave. I find the Biot and squirt flow to appear around approximately the same frequencies for this example.

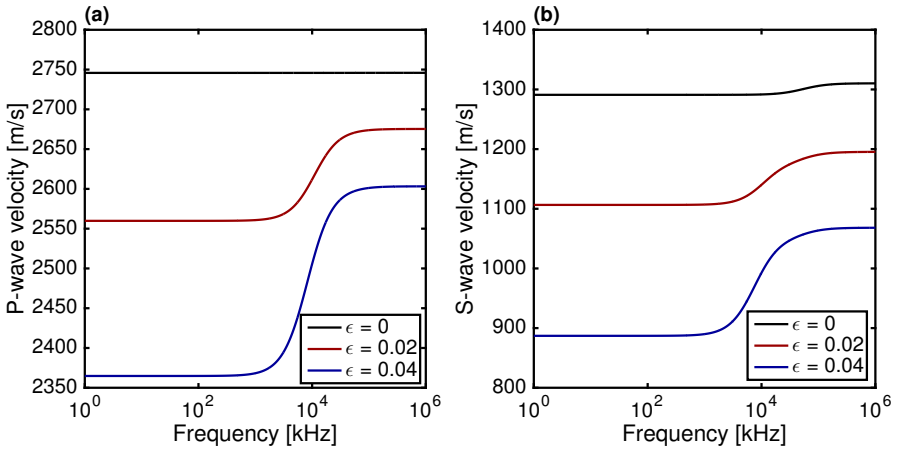

Figure 3.1: Effective P- (a) and S-wave (b) velocity dispersion for a poroelastic formation containing stiff and compliant ellipsoidal pores (see Table 3.1, slow formation). The black, red and blue lines correspond to crack densities of $\epsilon = 0, 0.02$ and 0.04, respectively, equivalent to crack porosities of $\phi_c = 0, 0.008$ and 0.016%. The crack density of $\epsilon = 0$ refers to the case with no squirt flow, which shows that the dispersion caused by Biot flow alone is small in this example. When compliant pores are present, resulting in squirt flow, red and blue lines, substantial dispersion appears for both the P- and the S-wave formation velocities.

The synthetic seismograms created with a 7.5-kHz monopole source for the different crack densities but at equal offset (Figure 3.2a) show the amplitude of the leaky-P mode package to increase while the Stoneley wave decreases in amplitude as a function of increasing crack density. In Figure 3.2b, the 13-receiver common-source gather is displayed for the formation with crack density of $\epsilon = 0.02$. The waveforms have been normalized with respect to the highest amplitude of the first receiver waveform and multiplied by half of the inter-receiver distance to fit with their respective receiver offsets. To analyze the waveforms further I applied the weighted spectral semblance (WSS) method (Nolte and Huang, 1997) to the 13-receiver common-source gather for the three different crack densities. The dispersion for crack densities $\epsilon = 0, 0.02$ and 0.04 (Figure 3.2c,d and e) show that the WSS used on the waveforms, excluding the Stoneley wave mode, correlates well with the effective formation P-wave dispersion results from Figure 3.1, shown as white lines. Warmer colors represent higher values for the weighted semblance function.

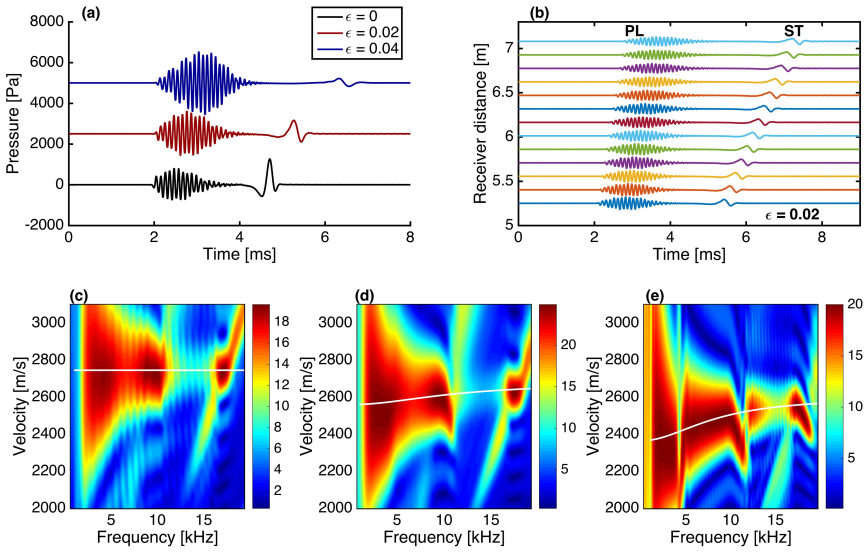

Figure 3.2: (a) Comparison of waveforms with a 7.5-kHz monopole source in the slow formation with a permeable borehole wall (see Table 3.1, slow formation) with equal offset at $z = 5.25$ m for the different crack densities. Crack densities of $\epsilon = 0.02$ and $\epsilon = 0.04$ have been moved upwards 2500 and 5000 Pa, respectively. The waveforms contain compressional, leaky-P and Stoneley wavemodes. The leaky-P amplitude increases while the Stoneley wave amplitude decreases with increasing crack density. (b) A 13-receiver common-source gather displaying the moveout of the leaky-P and the Stoneley wavemodes in the formation with $\epsilon = 0.02$. P-wave dispersion (d, e and f) computed from weighted spectral semblance method (WSS) (Nolte and Huang, 1997) for the 13-receiver common-source gather, excluding the Stoneley wave, for crack densities of $\epsilon = 0$ (d), $\epsilon = 0.02$ (e) and $\epsilon = 0.04$ (f). Warmer colors represent a higher likelihood for a specific frequency to travel at a specific velocity. The overlain white line corresponds to the effective formation P-wave velocity dispersion shown in Figure 3.1 for frequencies 1-20 kHz. Squirt flow clearly affects the dispersion of the leaky-P mode.

In Figure 3.3 the same results as in Figure 3.2 are shown but instead using a 1-kHz source. WSS applied to the 13 receiver common source gathers for the different crack densities (Figure 3.3c, d and e) displays relatively well defined dispersion. The results follow the phase-velocity dispersion by solving the period equation $\det\mathbf{M}(k_z, \omega) = 0$ for the Stoneley wave modes shown as white lines.

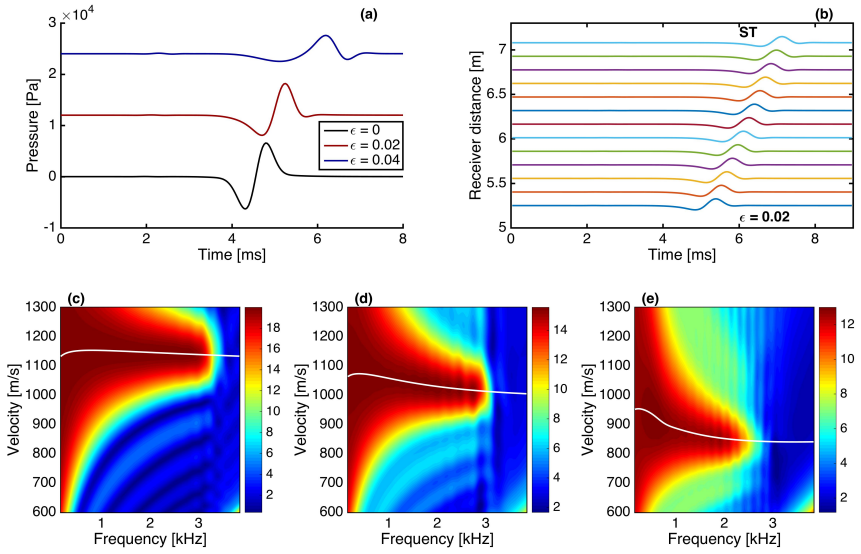

Figure 3.3: (a and b) Same as Figure 3.2 but using a 1-kHz monopole source. The 13-receiver common-source gather was processed with WSS over the full time interval for crack densities of $\epsilon = 0$ (c), $\epsilon = 0.02$ (d) and $\epsilon = 0.04$ (e). The white lines correspond to the Stoneley wave velocities obtained from solving the period equation using the Newton-Raphson method for each crack density (Tang and Cheng, 2004).

A comparison is shown in Figure 3.4a for the Stoneley wave mode phase-velocity dispersion for the three crack densities but holding the permeability

constant. With increasing crack density, the Stoneley wave phase velocity decreases. Similar results are found for impermeable borehole walls (Chen et al., 2014). I also display the Stoneley wave phase velocity dispersion for three different permeabilities while instead keeping crack density constant (3.4b). To separate formation compressional- and shear-wave velocity versus the slow-P wave velocity alterations on the Stoneley wave, I also compute the slow-P wave dispersion for the same formations (Figure 3.4c and d). I find the slow-P wave dispersion to be relatively insensitive to the crack density change. Thus, the rather substantial Stoneley wave phase velocity difference with crack density (Figure 3.4a) is largely due to the changes in formation P- and S-wave velocities and not due to additional fluid mobility.

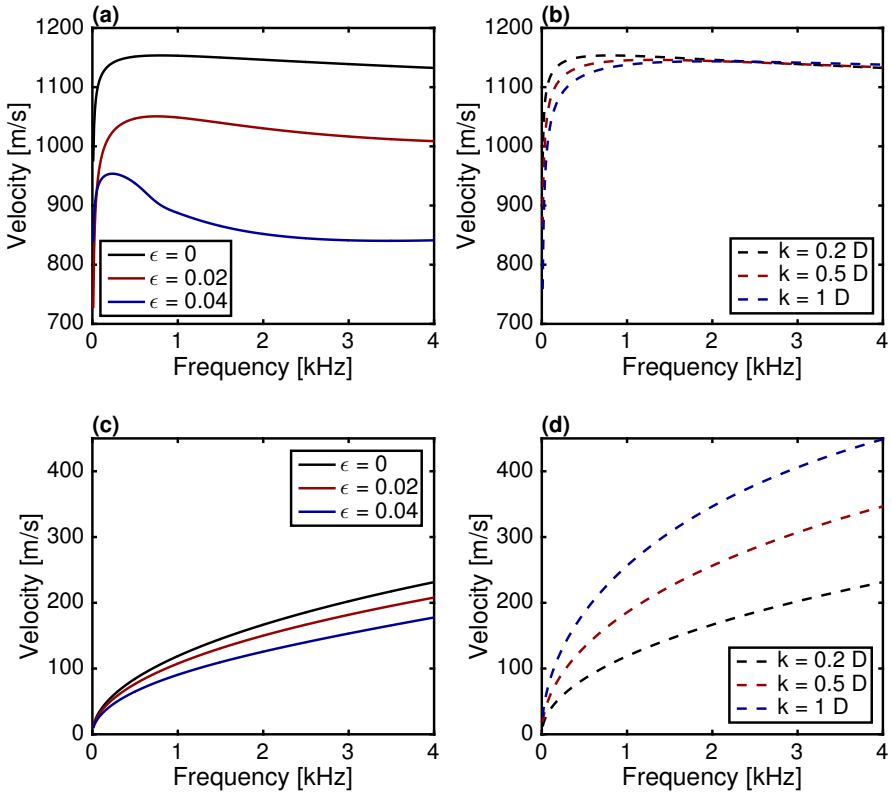

Figure 3.4: Stoneley and slow-P wave (a and c) dispersion comparison for the poroelastic slow formation with a permeable borehole wall containing crack densities of $\epsilon = 0, 0.02$ and 0.04, black, red and blue lines, all with permeability of 0.2 D. (b and d) Stoneley and slow-P wave dispersion for $\epsilon = 0$ but with permeabilities of $0.2, 0.5$ and 1D, black, red and blue lines.

3.4.2 Fast formation

When the formation S-wave velocity is faster then the borehole fluid P-wave velocity (fast formation), four wave modes are present in the full waveforms (Cheng and Toksöz, 1981; Tang and Cheng, 2004). They are the P- and S-wave modes together with the guided Stoneley and pseudo-Rayleigh waves. The pseudo-Rayleigh wave travels at velocities bounded above by the S-wave velocity and from below by the borehole fluid velocity. Figure 3.5 shows formation P- and S-wave velocities as a function of frequency for crack densities $\epsilon = 0, 0.04$ and 0.08 corresponding to crack porosities of $\phi_c = 0, 0.00168$ and 0.00335%. I again see little dispersion for the crack density of $\epsilon = 0$ corresponding to Biot flow. If I introduce compliant pores, corresponding to crack densities $\epsilon = 0.04$ and 0.08, I find more than 400 m/s dispersion for the P-wave and around 200 m/s velocity difference for the S-wave looking at the higher of the two crack densities (blue lines).

The full-waveform comparisons for equal offset but different crack densities (Figure 3.6a) display a slight increase in amplitude for the P-wave, while the pseudo-Rayleigh and Stoneley wave packet decreases in amplitude with increasing crack density. The waveforms with crack density of $\epsilon = 0.04$ and 0.08 have been moved upwards 1200 and 2400 Pa, respectively, for comparison purposes. The 13-receiver common-source gather for the fast formation with crack density of $\epsilon = 0.04$ (Figure 3.6b) shows the respective moveout for the P-, S-, pseudo-Rayleigh and Stoneley waves. The waveforms have been normalized similar to the slow formation waveforms in Figure 3.2b. In Figures

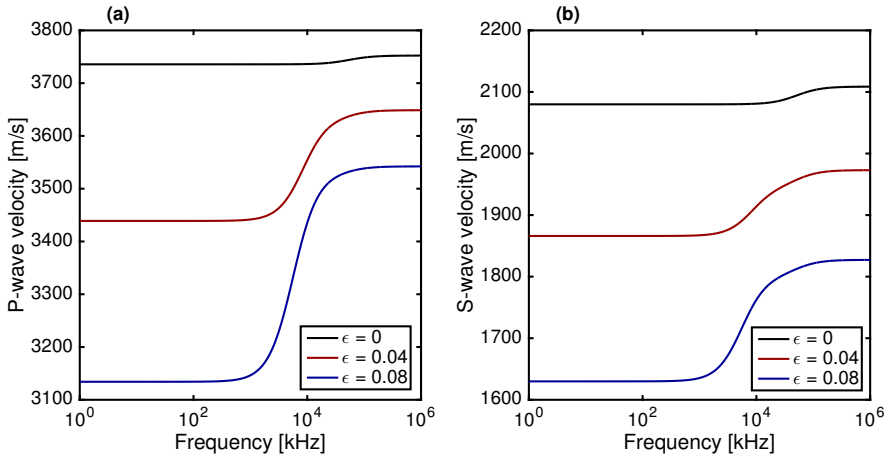

Figure 3.5: Effective P- (a) and S-wave (b) poroelastic formation velocities with crack densities $\epsilon = 0, 0.04$ and 0.08, corresponding to crack porosities of $\phi_c = 0, 0.016$ and 0.032% black, red and blue lines, respectively (see Table 3.1, fast formation).

3.6c, d, e and Figures 3.7a, b and c I attempt to isolate the P- and S-waves by only processing the waveforms over their respective appearance in time. For the P-wave I can infer some differences in the semblances due to the different crack densities that are in relatively good agreement with their respective formation P-wave dispersion in Figure 3.6, which are overlain in white. I also see some aliasing that is typical for WSS. This could possibly be resolved by applying a combined Prony and WSS method developed by Ma et al. (2010).

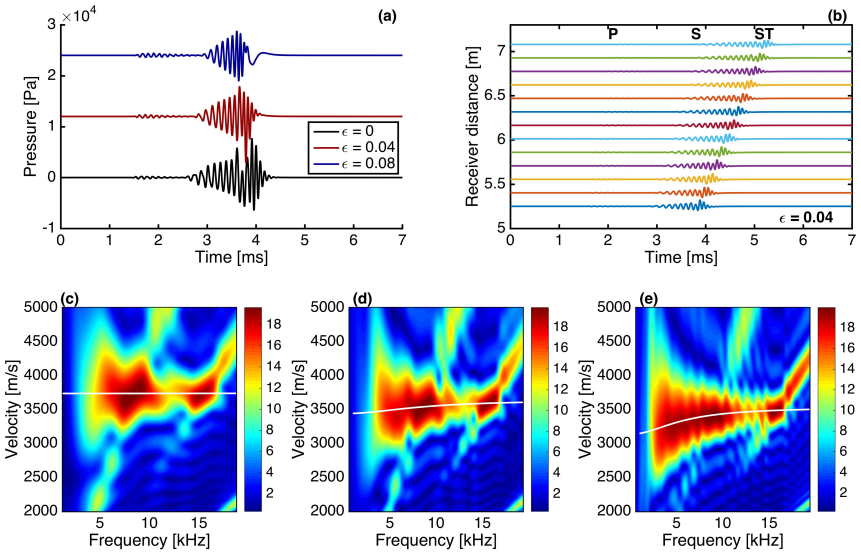

Figure 3.6: Synthetic miscroseismograms (a and b) created with a 7.5-kHz monopole source for a water-filled permeable borehole of radius 12-cm surrounded by a poroelastic fast formation with stiff and compliant pores (see Table 3.1, fast formation). In (a) the waveforms have a constant offset of z=5.25 m but contain different crack densities. The waveforms contain P, S and Stoneley wave modes. They also contain the high-frequency dispersive wave packet after the S-wave referred to as the pseudo-Rayleigh wave (Tang and Cheng, 2004). (b) A 13-receiver common-source gather through the formation with crack density of $\epsilon = 0.04$. P-wave dispersion (c,d and e) using WSS applied to the 13-receiver common-source gather in the fast formation containing crack densities of $\epsilon = 0, 0.04$ and 0.08, for 0-2.5 ms. The white lines correspond to the effective formation P-wave velocities shown in Figure 3.5.

The S-wave dispersion results from WSS (Figure 3.7a, b and c) do not correlate well with their respective formation dispersions in white for any of the crack densities. This might be due to interference from the pseudo-Rayleigh waves, which are difficult to exclude from the specific time interval. If I process the entire waveforms with WSS I find clear appearance of the Stoneley and the pseudo-Rayleigh wave in the 0-5 kHz and 5-20 kHz range (Figure 3.7d, e and f). The white lines correspond to the the phase velocity of respective wave mode and formation by again solving the period equation.

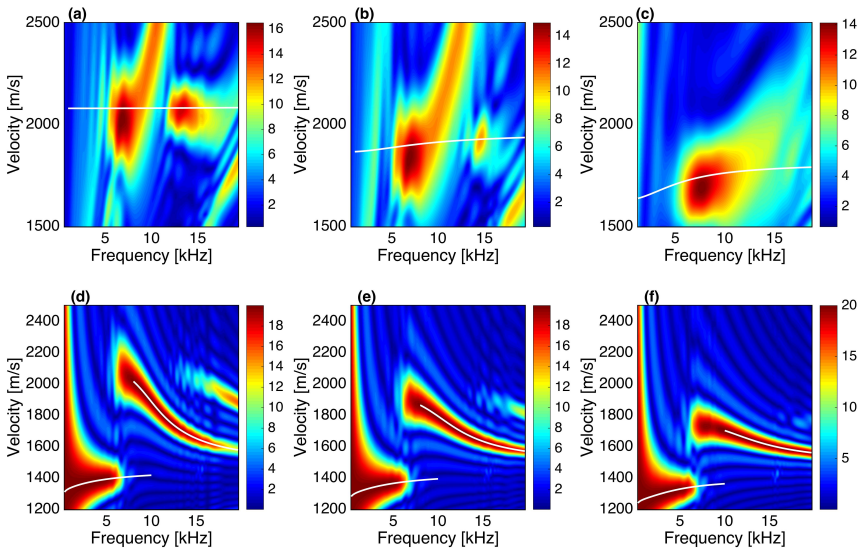

Figure 3.7: S-wave dispersion (a, b and c) derived from WSS for the 13-receiver common-source gather in the fast formation at around 2-3.7 ms containing crack densities of $\epsilon = 0, 0.04$ and 0.08. White lines correspond to the effective formation S-wave velocities shown in Figure 3.5. The discrepancy between the velocity results from WSS and the formation velocity might be explained by interference of the pseudo-Rayleigh wave that travels at the S-wave velocity at the cutoff frequency to approach the borehole-fluid velocity at high frequencies (Tang and Cheng, 2004). (d, e and f) WSS applied over 0-6 ms for crack densities $0, 0.04$ and 0.08. The 0-5 kHz region is dominated by Stoneley waves, and the 5-20 kHz region corresponds to the pseudo-Rayleigh waves. The white lines correspond to the solution of the period equation for the Stoneley and pseudo-Rayleigh waves phase velocities.

In Figure 3.8 I display the pseudo-Rayleigh phase velocity in solid lines for the different crack densities together with their respective formation S-wave velocities. I find the pseudo-Rayleigh phase velocities to be bounded by the formation S-wave velocities at their specific cuttoff frequencies, following the shear-wave dispersion of the formations.

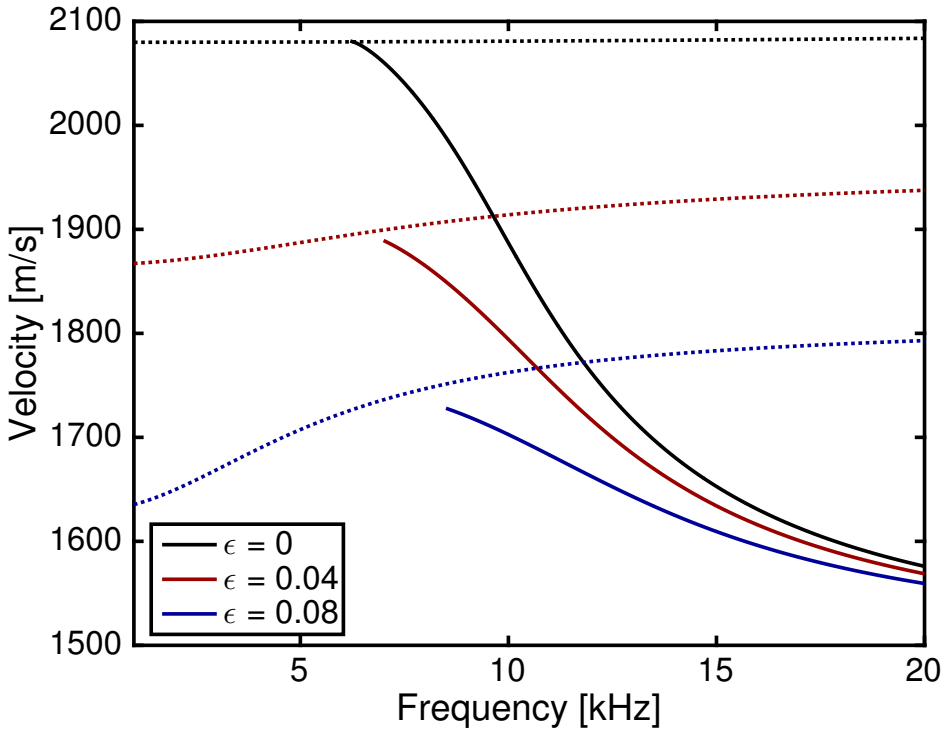

Figure 3.8: Pseudo-Rayleigh wave dispersion comparison (solid lines) for the fast formation with different crack densities, with respective effective S-wave formation velocities (dotted lines). I find the pseudo-Rayleigh waves to travel at approximately the S-wave velocities at their cut-off frequencies.

In Figure 3.9a I show the common receiver gather using a 1-kHz monopole source in the fast formation. The Stoneley wave does not appear to be as af-

fected by the change in crack densities as for the slow formation (Figure 3.3a), perhaps due to less efficient coupling to the formation. A good match is found between the WSS results and the solution to the period equation for all different crack densities (see Figure 3.9c, d and e).

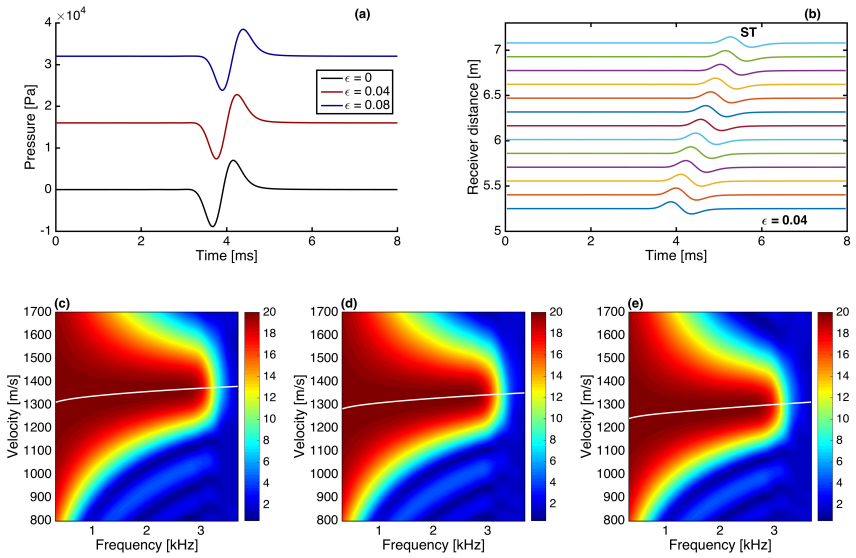

Figure 3.9: (a and b) Same as Figure 3.6 but using a 1-kHz monopole source. Stoneley-wave mode dispersion for crack densities of $\epsilon = 0$ (c), $\epsilon = 0.04$ (d) and $\epsilon = 0.08$ (e). The white lines corresponding to the Stoneley wave velocities come from solving the period equation with the Newton-Raphson method follow the results of WSS method well.

The phase velocity dispersion results from Figure 3.9 are combined in Figure 3.10a and compared with the results of holding the crack density constant but changing permeability (Figure 3.10b). I find a larger velocity effect due to change in crack density than due to a change in permeability. Because the slow-P wave velocities barely change with increasing crack density (Figure

3.10c), I again conclude this effect is mainly through change in formation P- and S-wave velocity and not due to a change in fluid mobility.

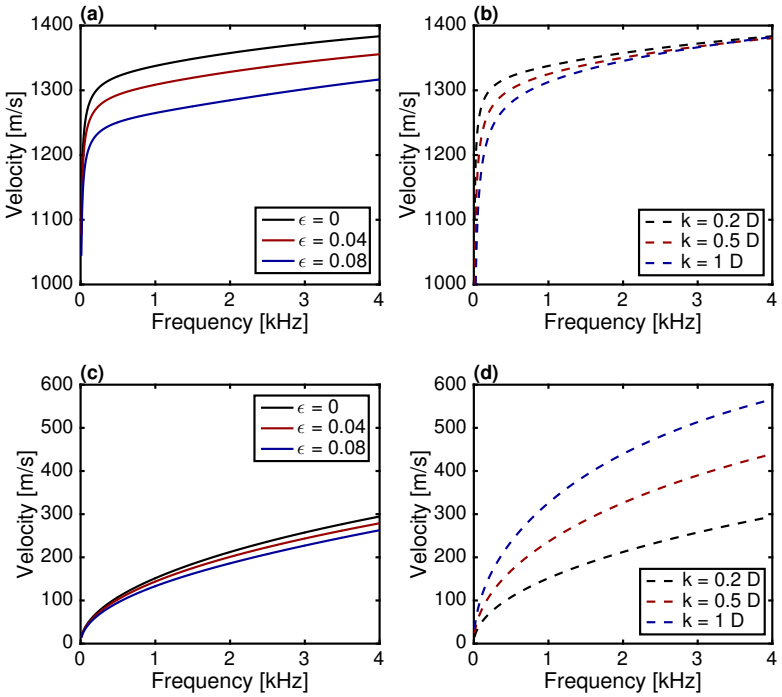

Figure 3.10: Stoneley-wave and slow-P wave (a and c) dispersion comparison for the poroelastic fast formation containing crack densities of $\epsilon = 0, 0.04$ and 0.08, black, red and blue line, but the same permeability, $k = 0.2$ D, respectively. In (b and d) I keep $\epsilon = 0$ but change permeability. There is not as much dispersion difference as in the slow formation example (Figure 3.4a) with changing crack densities.

3.5 Discussion

The numerical results demonstrate that both the P- and S- waves are sensitive to the squirt-flow mechanism in the 1-20 kHz frequency band. This effect in the form of dispersion is relatively clear for the P-wave in both slow and fast formations when processing the waveforms with WSS. It is, however, more difficult to infer the dispersion for the S-waves in the fast formation, most likely due to interference from the pseudo-Rayleigh wave modes. It does, however, exist and might be inferred from the pseudo-Rayleigh wave phase velocity at the cuttoff frequency. A common way to process monopole waveforms for velocity information is through time domain methods, e.g., STC (Kimball and Marzetta, 1986). However, Kimball (1998) showed that when a dispersive wave is processed nondispersively, one event can show up as two. Although this method was intended mostly for flexural-wave dispersion due to the geometry of the borehole, I find that WFF can create substantial P- and S-wave velocity dispersion. Thus a more thorough analysis of the P- and S-wave modes might be in order.

My results also show the Stoneley wave modes to be sensitive to squirt flow in both formations although more so for the slow formation than the fast formation. Several studies have attempted to estimate permeability using the Stoneley wave (e.g., Cheng et al., 1987; Kenneth et al., 1989; Tang et al., 1991), but none of them have corrected for the effect of squirt flow or compliant pores to my knowledge. I plan on comparing the unified model more thoroughly against different theories and real data in upcoming studies. Future work

could include a more realistic borehole structure to investigate the sensitivity of the different wavemodes to the fluid saturated compliant pores when, e.g., a tool is present.

3.6 Conclusions

This work presented a procedure to incorporate squirt flow into Biot's poroelastic theory using Chapman's frequency-dependent moduli in an attempt to unravel some of the complex interactions between solid and fluid in a dual-porosity medium. The unified wave equation was applied to both a slow and a fast formation to study the effect of fluid-saturated compliant pores resulting in a less stiff rock and squirt flow on borehole acoustic wavemodes excited by a monopole source. I found that compliant pores can have a substantial effect on both the P- and S- wave modes in both slow and fast formations. The compliant pores decreased the velocities and caused significant dispersion for both modes. The Stoneley wave was also significantly affected by the presence of compliant pores, both in amplitude and phase-velocity dispersion, more so for slow formations then for fast, indicating the sensitivity is mostly due to the formation P- and S-wave velocity changes and not due to fluid mobility changes.

Chapter 4

Local and global fluid-flow effects on flexural wave modes

4.1 Abstract

Wave-induced fluid flow (WIFF) can significantly alter the effective formation velocities and cause increasing waveform dispersion and attenuation. In this work, I use modified frame moduli from the theory of Chapman together with the classical theory of Biot to improve our understanding of local- and global-flow effects on dipole flexural wave modes in boreholes. I investigate both a slow and a fast formation with and without compliant pores, which induce local flow. The discrete wavenumber summation method generates the waveforms, which are then processed with the weighted spectral semblance (WSS) method to compare with the solution of the period equation. I find compliant pores to decrease the resulting effective formation P- and S-wave velocities, which in turn decrease the low-frequency velocity limit of the flexural wave. Furthermore, depending on the frequency at which the local-flow dispersion occurs, different S-wave velocity predictions from the flexural wave become possible. This issue is investigated through changing the local-flow critical frequency. Sensitivity analyses of the flexural wave phase velocity to small changes in WIFF parameters show the modeling to be mostly sensitive

to compliant pores in both slow and fast formations.

4.2 Introduction

Accurate shear-wave velocity measurements are of great importance in petroleum reservoir exploration, reserve estimation, hydrocarbon production and well completion, including apllications to seismic-well ties, fluid substitution, pore pressure predictions and wellbore stability (Tang and Cheng, 2004). White (1967) first proposed the idea of using dipole sources in boreholes to acquire knowledge of the formation shear-wave velocities. The dipole source excites a borehole-surface guided wave, which is referred to as the flexural wave. The flexural-wave mode is naturally dispersive due to the geometry of the borehole. This phenomen is to be distinguished from dispersion resulting from, e.g., local or global fluid flow. In an isotropic elastic formation, the low frequency components (1-3 kHz) of the flexural wave travel at the speed of the formation S-wave velocity; the high-frequency components (6-10 kHz) of the flexural wave travel at the velocity of the high-frequency Stoneley wave (Kurkjian and Chang, 1986; Winbow, 1988; Tang and Cheng, 2004). Conventionally, acoustic waveforms are processed for velocities using time-domain methods such as slowness-time coherence (STC) (Kimball and Marzetta, 1986). However, when the wave modes are dispersive, the velocities obtained from STC are a weighted spectral average of the phase-velocity dispersion curves. For the flexural wave, STC predicts slower shear wave velocities than the true formation S-wave velocities (Kimball, 1998; Geeritz and

Tang, 2003). This error can be accounted for using dispersion-correction techniques. Dispersion-correction methods can be categorized as data driven or model based. Data-driven models do not use full theoretical modeling, but they do assume that in the low-frequency regime, the flexural wave phase-velocity dispersion becomes flat and reaches the S-wave formation velocity (Huang and Yin, 2005; Tang et al., 2010). The data-driven methods become invalid when the low-frequency components of the flexural wave have relatively small excitation or when the signal-to-noise ratio becomes too small. Model-based methods have the advantage that they do not specifically require the low-frequency flexural wave data because they instead predict the S-wave velocities by fitting the actual data-dispersion curve with a theoretical model dispersion curve (Kimball, 1998; Geeritz and Tang, 2003; Lee et al., 2016). However, model-based inversions will work well only if the theoretical model is an accurate description of real wave propagation. Therefore, it is important to study the complex interaction of the flexural wave with different types of formations. The flexural wave has been numerically simulated in a multitude of borehole scenarios, e.g., boreholes surrounded by isotropic formations (Winbow, 1988; Kurkjian and Chang, 1986), cased boreholes (Schmitt, 1993), nonaxisymmetric boreholes (Randall, 1991), boreholes with eccentred tools (Schmitt, 1993; Pardo et al., 2013), transversely isotropic formations (Leslie and Randall, 1992; Zhang, 2013), in the presence of stress-induced formation anisotropy (Liu and Sinha, 2000, 2003) and deviated boreholes with anisotropic formations (Sinha et al., 2006; He et al., 2010; Mallan et al., 2011).

Most formations of economic interest in exploration contain mobile fluids that are thought to act as the main contributors to seismic attenuation and dispersion (Mavko et al., 2009; Müller et al., 2010). When a seismic wave passes through a fluid-saturated porous formation, pressure gradients appear on a variety of different length scales. The pressure gradients at the seismic-wavelength scale, resulting from inertial and viscous forces coupling the fluid to the solid movement, can be described by the classical theory of Biot (1956a,b). The resulting wave-induced fluid flow (WIFF) commonly is referred to as global or macroscopic flow due to neglecting details of the pore space and local flow. The effect of global flow on flexural waves has been studied using an isotropic poroelastic formation (Schmitt, 1988d), a transversely isotropic formation (Schmitt, 1989) and a poroelastic formation with an anisotropic permeability (He et al., 2013). Global flow does not affect the phase-velocity dispersion of the flexural wave to any significant extent (Schmitt, 1988d). However, when a seismic wave propagates through a medium containing a distribution of both stiff and compliant pores, the wave will cause an uneven amount of deformation of the compliant versus the stiff pores resulting in local pressure gradients. If the wave propagates at lower frequencies than the critical frequency at which the dispersion phenomenon occurs, the fluid in the compliant pore space will have time to equilibrate with the fluid in the stiff pores. If the wave travels at higher frequencies relative to the critical frequency, the fluids in the compliant pore space will be trapped. The resulting effect is an observed stiffer rock with faster apparent seismic velocities.

This pore-space WIFF is often referred to as squirt flow or local flow (Müller et al., 2010). Chen et al. (2014) found using the Tang et al. (2012) cracked, porous-medium, elastic-wave theory in a tight formation that the presence of cracks affected the flexural wave. To the best of my knowledge, this is the only other study addressing the combined effect of global and local flow on flexural waves besides ours. My study differs from previous work in the unification of global and local flow and in that I analyze the dispersion of the computed waveforms using weighted spectral semblance (WSS) (Nolte and Huang, 1997) and by solving the period equation for dispersion (Tang and Cheng, 2004). In addition, Chen et al. (2014) focused on tight formations whereas I analyze fluid-saturated fast and slow formations, similar to the those presented in Schmitt (1988c).

The purpose of this study is to investigate the combined effects of squirt flow and Biot flow on flexural waves with emphasis on squirt flow. I use the combined theory of Chapman et al. (2002) incorporated into Biot (1956a) poroelastic theory presented in Dahl and Spikes (2017). Similar to the work presented in Dahl and Spikes (2017), this study is ideal where I neglect a tool response, borehole rugosity and dipping layers. However, it is still of importance to understand the isolated effect of compliant pores on flexural wave modes before adding additional borehole complexities. I simulate flexural waves in two different formations, one slow and one fast, both containing different quantities of compliant pores. I then analyze the waveforms using WSS alongside the phase- and group-velocity dispersion from solutions of the

period equation.

4.3 Theory

4.3.1 Effective rock frame moduli

Dahl and Spikes (2017) used the theory of Chapman et al. (2002) to find an expression for the modified rock-frame moduli containing dry stiff- and fluid-saturated compliant pores. Due to the fluid-filled microcracks, both the shear- and bulk-frame moduli become frequency dependent. These frequency-dependent moduli are used in Biot (1956a) instead of the dry-frame moduli to add the effect of squirt flow to Biot flow. I present the main results of the theory in this section.

To calculate the effective bulk and shear moduli for a dual porosity medium containing compliant ellipsoidal microcracks with small aspect ratios and stiff spherical pores, Chapman used the interaction energy approach of Eshelby (1957), which gives

$$K_{eff} = K_m - \frac{K_m^2}{\sigma^2} \sum_t \phi_t (\epsilon_{ij}^t \sigma_{kl}^0 - \sigma_{ij}^t \epsilon_{kl}^0), \tag{4.1}$$

and

$$\mu_{eff} = \mu_m - \frac{\mu_m^2}{\sigma^2} \sum_t \phi_t (\epsilon_{ij}^t \sigma_{kl}^0 - \sigma_{ij}^t \epsilon_{kl}^0), \tag{4.2}$$

for the effective bulk and shear moduli. In Equations 4.1 and 4.2, K_m and μ_m refer to mineral bulk and shear moduli, respectively, ϕ_t to the different quantities of fractional porosities, σ is the applied external stress, σ_{kl}^0 and ϵ_{kl}^0

denote the stresses and strains in the matrix and σ_{ij}^t and ϵ_{ij}^t denote the stresses and strains in the different pore spaces.

The stress in the pore space is set to $\sigma_{ij}^t = 0$ in Equations 4.1 and 4.2 to calculate expressions for the dry effective moduli for the rock containing stiff pores and ellipsoidal microcracks with small aspect ratios. Following Chapman et al. (2002) and Chapman (2003) the dry moduli are in the form of

$$K_{dry} = K_{dry}^* - K_m^2 \frac{\phi_c}{\sigma_c}, \tag{4.3}$$

and

$$\mu_{dry} = \mu_{dry}^* - \mu_m (\frac{4\mu_m}{15\sigma_c} + \frac{8(1-\nu)}{5(2-\nu)\pi r})\phi_c, \tag{4.4}$$

where K_{dry}^* and μ_{dry}^* refer to the dry-rock moduli without compliant pores. In Equations 4.3 and 4.4, ϕ_p and ϕ_c denote the stiff and compliant porosity, the parameter $\sigma_c = \pi\mu_m r/(2(1-\nu))$, with r being the aspect ratio of the microcracks and ν is the Poisson's ratio of the mineral matrix.

To add the fluid to the compliant pores, thus making the effective frame moduli frequency dependent, the stress in the compliant pore space is instead set to $\sigma_{ij}^c = P_c(\omega)$ and $\sigma_{ij}^t = 0$ for all other t in Equations 4.1 and 4.2. Then $P_c(\omega)$ refers to the frequency-dependent fluid pressure in the microcracks. Solving for pressure $P_c(\omega)$, and assuming a uniform distribution of normal crack directions, the effective frequency-dependent rock moduli containing dry stiff pores and fluid-saturated compliant microcracks are

$$K_b(\omega) = \text{Real}(K_{dry} + \phi_c(\frac{K_m^2}{\sigma_c} + K_m)(C_1(\omega) + 3C_2(\omega))) \tag{4.5}$$

and

$$\mu_b(\omega) = \text{Real}(\mu_{dry} + \phi_c \frac{4\mu_m^2 C_1(\omega)}{15\sigma_c}). \tag{4.6}$$

The K_{dry} and μ_{dry} are given in Equations 4.3 and 4.4, and the coefficients $C_1(\omega)$ and $C_2(\omega)$ can be found in Appendix A.

4.3.2 Poroelastic wave equation with modified frequency-dependent frame moduli

I describe the formation surrounding the borehole using the Biot (1956a) poroelastic wave equation,

$$(A+\mu)\nabla\nabla\cdot\mathbf{u} + \mu\nabla^2\mathbf{u} + Q\nabla\nabla\cdot\mathbf{U} = \rho_{11}\ddot{\mathbf{u}} + \rho_{12}\ddot{\mathbf{U}} + b(\dot{\mathbf{u}} - \dot{\mathbf{U}}), \tag{4.7}$$

$$Q\nabla\nabla\cdot\mathbf{u} + R\nabla\nabla\cdot\mathbf{U} = \rho_{12}\ddot{\mathbf{u}} + \rho_{22}\ddot{\mathbf{U}} - b(\dot{\mathbf{u}} - \dot{\mathbf{U}}), \tag{4.8}$$

where I exchange the dry moduli with the frequency-dependent modified-frame moduli from equations 4.5 and 4.6 in the expressions for the elastic coefficients A, μ, Q, and R in equations C.13 to C.16. In Equation 4.7 and 4.8, $\mathbf{u}$ and $\mathbf{U}$ are the average displacement vectors in the solid and the fluid phases, respectively, and $\rho_{11} = (1-\phi)\rho_m - (1-\alpha)\phi\rho_f$, $\rho_{22} = \alpha\phi\rho_f$ and $\rho_{12} = (1-\alpha)\phi\rho_f$, where ρ_m and ρ_f are the densities of the mineral and the fluid, ϕ refers to the total porosity, α is the tortuosity and $b = \eta\phi^2/k$, where η is the viscosity of the fluid and k is the permeability of the rock (Biot, 1956a; Plona and Johnson, 1980; Mavko et al., 2009). Biot's wave equation in cylindrical coordinates is solved by dividing the average displacement vectors into the fast and slow compressional waves, $\Phi_{f,s}$, together with the SH- and SV-type shear-wave

displacement potentials, Ψ and Γ (e.g., Schmitt, 1988d; Tang and Cheng, 2004) resulting in the vectors,

$$\mathbf{u} = \nabla\Phi_f + \nabla\Phi_s + \nabla \times (\Psi \mathbf{e}_z) + \nabla \times \nabla \times (\Gamma \mathbf{e}_z), \tag{4.9}$$

$$\mathbf{U} = \mu_f \nabla\Phi_f + \mu_s \nabla\Phi_s + \alpha_0 \nabla \times (\Psi \mathbf{e}_z) + \alpha_0 \nabla \times \nabla \times (\Gamma \mathbf{e}_z). \tag{4.10}$$

In Equation 4.9 and 4.10, $\mathbf{e}_z$ refers to the unit vector in the vertical direction. Using Equations 4.9 and 4.10 in Biot's wave equation (Equations 4.7 and 4.8) and solving for the different potentials in the frequency domain results in four Helmholtz equations. Those equations have respective complex wavenumbers $k_{f,s}$ and k_t, where k_f refers to the fast-, k_s to the slow P-wavenumber and k_t to the S-wavenumber. The wavenumbers, $k_{f,s}$ and k_t are given by Equations C.6 and C.7. The expressions for the different potentials are given in, e.g., Schmitt (1988d). To couple the different poroelastic displacement potentials to the borehole-fluid potential, I apply boundary conditions for a permeable borehole wall in cylindrical coordinates. The boundary conditions used at the borehole wall are a balance of fluid volume, continuity of radial stress, zero azimuthal, $\sigma_{r\theta}$, and tangential, σ_{rz}, stresses in the solid and equal pressure,

$$\begin{cases} v_f = u_r + \phi(U_r - u_r), \\ \sigma_{rr}^{(fl)} = \sigma_{rr} + s, \\ 0 = \sigma_{r\theta}, \\ 0 = \sigma_{rz}, \\ \sigma_{rr}^{(fl)} = s/\phi. \end{cases} \tag{4.11}$$

In Equation 4.11, v_f refers to the borehole fluid radial displacement, $\sigma_{rr}^{(fl)}$ is the borehole fluid radial stress, σ_{rr} is the solid radial stress and s is the

tension in the pore fluid given in Biot (1962a). For descriptions on how to calculate these, see, e.g., Schmitt (1988d) or Tang and Cheng (2004). Using the expressions for the average displacement vectors and stresses related to the displacement potentials in the boundary conditions of equations 4.11, I find the linear system of equations

$$\mathbf{M}\bar{\mathbf{x}} = \bar{\mathbf{b}} \tag{4.12}$$

where the matrix $\mathbf{M}$ and the vector $\bar{\mathbf{b}}$ are given in Appendix B and $\bar{\mathbf{x}} = [\tilde{A}_{fl}^{(n)}, \tilde{A}_{f}^{(n)}, \tilde{A}_{s}^{(n)}, \tilde{B}^{(n)}, \tilde{C}^{(n)}]^{\mathrm{T}}$, setting $n = 1$ for a dipole source. The coefficients $\tilde{A}_{f}^{(n)}, \tilde{A}_{s}^{(n)}$ describe the fast and slow compressional waves, and $\tilde{B}^{(n)}, \tilde{C}^{(n)}$ the SH and the SV-type shear waves in the formation containing Biot and squirt flow, while $\tilde{A}_{fl}^{(n)}$, which gives the reflected/refracted borehole wall response, is used in the discrete wavenumber summation method to generate waveforms (e.g., Cheng and Toksöz, 1981; Tang and Cheng, 2004).

To understand the complex interaction between the parameters and the flexural wave-mode phase velocity dispersion, the elasticity or sensitivity of the function defined as (Tang and Cheng, 2004; Yang et al., 2011),

$$S(f,p) = \frac{p}{V_{phase}(f)} \frac{\delta V_{phase}(f)}{\delta p} \tag{4.13}$$

is also investigated. In equation 4.13, $V_{phase}(f)$ is the phase velocity and p is the parameter of interest. I solve the partial derivative using the Euler forward with a stepsize of $0.1\%p$. The sensitivity can be thought of as the 0.1 percent change in phase velocity due to a 0.1% change in a given parameter (Schmitt, 1989).

4.4 Numerical examples

This section investigates the effect of local and global flow on flexural waves in fluid-filled boreholes with emphasis on local flow. I consider two different formations, a fast and a slow, similar to the ones presented in Schmitt (1988c) and Dahl and Spikes (2017) with fluid-saturated stiff and compliant pores. Table 4.1 contains the rock-property values, and the fluid in the pore space together with the borehole is assumed to be water (see Table 4.2). The borehole radius is set to $R = 12$ cm, with the source to first receiver distance being $z_1 = 3$ m, and the distance in between receivers is $\Delta z = 0.1524$ m. I use 13 receivers with a dipole source generating a Ricker wavelet with center angular frequency of $\omega_0 = 2\pi \cdot 3$ kHz.

4.4.1 Slow formation

Figure 4.1 shows the effective formation P- and S-wave velocities in the slow formation as I change the crack density from $\epsilon = 0$, corresponding to only Biot flow present, to $\epsilon = 0.02$ where both Biot and squirt flow are apparent. I find that for the slow formation, Biot flow accounts for little to no P-wave dispersion whereas it contributes somewhat to the S-wave dispersion. When I include compliant pores, I find the low-frequency velocities to decrease together with substantial P- and S-wave velocity dispersion. For the S-wave velocity I see two critical frequencies where velocity increases. The first one corresponds to squirt flow, and the second increase is due to Biot flow.

The dipole common-receiver waveforms generated in the slow formation

Table 4.1: Parameters for porous, slow and fast formations containing compliant pores. The terms K_m, μ_m and ρ_m are the mineral grain bulk and shear moduli and density. Here, K^*_{dry} and μ^*_{dry} are the dry porous rock bulk and shear moduli excluding the compliant pores, and ϕ_s, ϵ and ϕ_c are the stiff porosity, the crack density and the compliant porosity, calculated from the crack density. Terms k and α are the permeability and tortuosity, respectively. For a random system, $\alpha = 3$ (Stoll, 1977). The aspect ratio is denoted r, and the timescale parameter τ. An estimate is $\tau \approx 10^{-5}$ s for water-saturated sandstone (Chapman, 2001).

Slow formation					
K_m [GPa]	μ_m [GPa]	ρ_m [kg/m^3]	K^*_{dry} [GPa]	μ^*_{dry} [GPa]	ϕ_s [%]
35	32	2600	5.5	3.8	20
ϵ [−]	ϕ_c [%]	k [D]	α [−]	r [−]	τ [s]
0-0.02	0-0.00084	0.2	3	10^{-4}	$10^{-4.3}$
Fast formation					
K_m [GPa]	μ_m [GPa]	ρ_m [kg/m^3]	K^*_{dry} [GPa]	μ^*_{dry} [GPa]	ϕ_s [%]
37.9	32	2650	15.4	10.1	19
ϵ [−]	ϕ_c [%]	k [D]	α [−]	r [−]	τ [s]
0-0.08	0-0.00335	0.2	3	10^{-4}	10^{-5}

Table 4.2: Parameters for the borehole and saturating fluid. The terms K_f, ρ_f and η are the bulk modulus, density and viscosity of the fluid, respectively.

K_f [GPa]	ρ_f [kg/m^3]	η [Pa · s]
2.25	10^3	10^{-3}

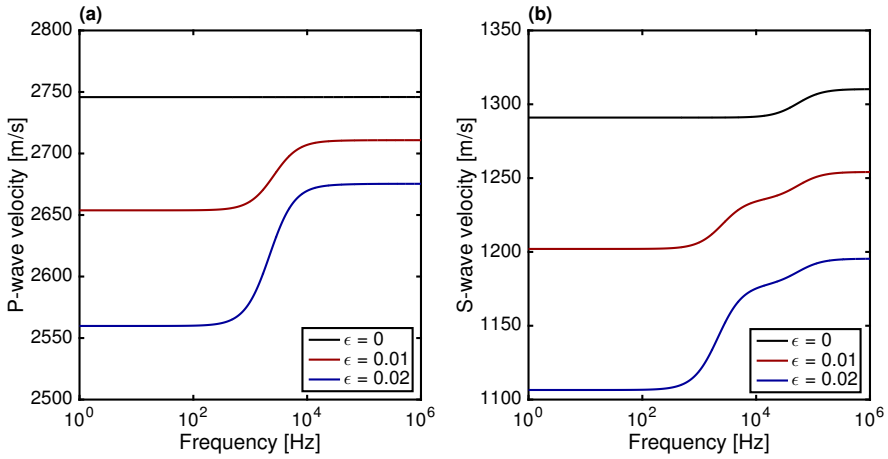

Figure 4.1: Frequency-dependent effective formation compressional (a) and shear-wave (b) velocities in the slow, poroelastic formation (see Table 4.1, slow formation) as a function of increasing crack density. The black line corresponds to $\epsilon = 0$, Biot flow only, the red line to crack density $\epsilon = 0.01$, Biot and squirt flow present, and the blue line corresponds to $\epsilon = 0.02$.

for different crack densities (Figure 4.2a) show the flexural-mode velocities and amplitudes to decrease as a function of increasing crack density relative to the case of $\epsilon = 0$.

In Figure 4.2b I display the normalized common-source gathers for the formation with crack density of $\epsilon = 0.01$. The gather contain the P and flexural modes. I analyze the 13 receiver common-source gather using WSS for the three different formations containing increasing crack density (Figure 4.3a-c). I have also overlain the effective formation S-wave velocities from Figure 4.1 together with the phase velocity dispersion for the flexural wave by solving the period equation, $\det\mathbf{M}(k_z, \omega) = 0$, using the Newton-Raphson method (Tang and Cheng, 2004) shown as white lines. Because the Biot-flow critical

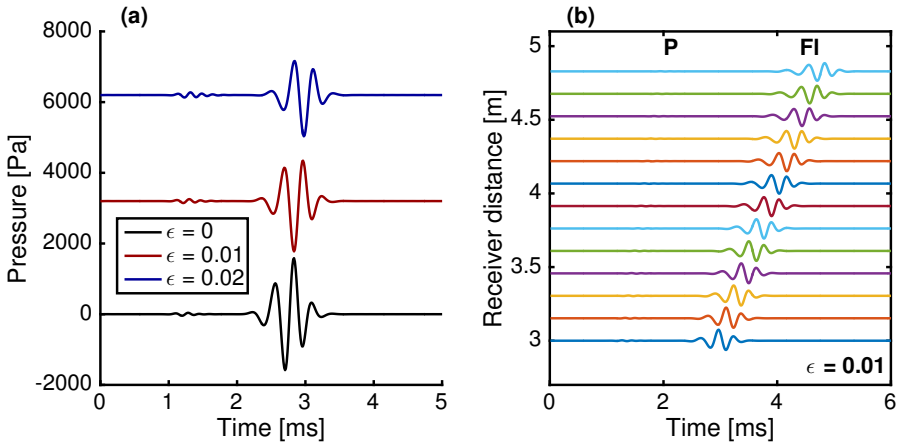

Figure 4.2: (a) Comparison of a 3 kHz dipole source common-receiver gather, $z = 3$m, in the slow formation with a permeable borehole wall using different crack densities, ϵ. The waveforms have been moved upwards for comparison purposes. (b) A 13-receiver common-source gather displaying the moveout of the P- and flexural-wave modes.

frequency is higher than the frequency range for the flexural wave, the effective formation S-wave dispersion appears flat (Figure 4.3a). Accordingly I could determine the S-wave velocity from the low-frequency part of the flexural wave rather easily. When I increase crack density, dispersion in the formation S-wave occurs. The low-frequency limit of the flexural wave follows the effective formation S-wave dispersion. For the flexural wave with crack density $\epsilon = 0.02$ (Figure 4.3c), I would most likely predict a velocity around 1140 m/s whereas the low-frequency effective S-wave velocity is around 1100 m/s.

I summarize the results from solving the period equation for phase- and group-velocities together with the effective formation S-wave velocities in Figure 4.4a. Both the phase and group velocities decrease as crack density

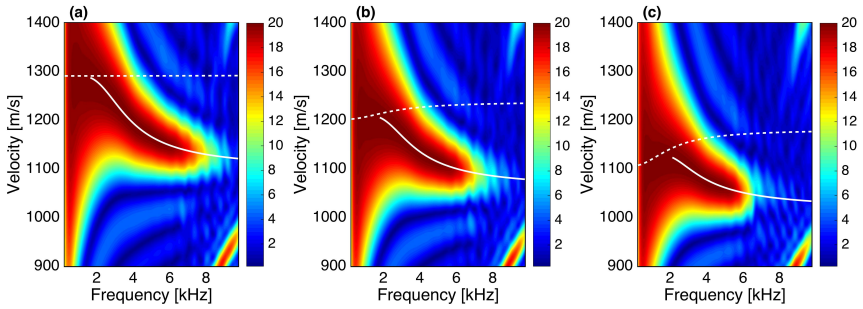

Figure 4.3: WSS dispersion analysis for the common-source gathers in the slow formation for crack densities $\epsilon = 0$ (a), $\epsilon = 0.01$ (b) and $\epsilon = 0.02$ (c). Overlain in white (dashed lines) are the effective formation S-wave velocities from Figure 4.1 and the flexural-wave mode phase-velocity dispersion (white solid lines) resulting from the solution to the period equation.

increases. The reason for the two velocities not to merge in the low-frequency regime is most likely due to interference of a branch point at the cutoff frequency (Schmitt, 1989). The Airy phase of the flexural wave, associated with the minimum of the group velocity, decreases with increasing crack density. The maximum onset of excitation is related to the Airy phase (Schmitt, 1988d) and explains why the flexural wave envelope arrives later in time when I add more compliant pores to the formation (see Figure 4.2a). Using the effective formation P- and S-wave velocity at the respective low-frequency cutoff for the flexural wave (Figure 4.4a), I solve the period equation for an isotropic elastic formation (solid lines) (e.g., Tang and Cheng, 2004). I then compare the phase-velocity dispersion with results from the combined WIFF model (solid lines) in Figure 4.4b. The combined versus elastic model-derived phase-velocity dispersion deviates increasingly as I add more compliant pores to the formation.

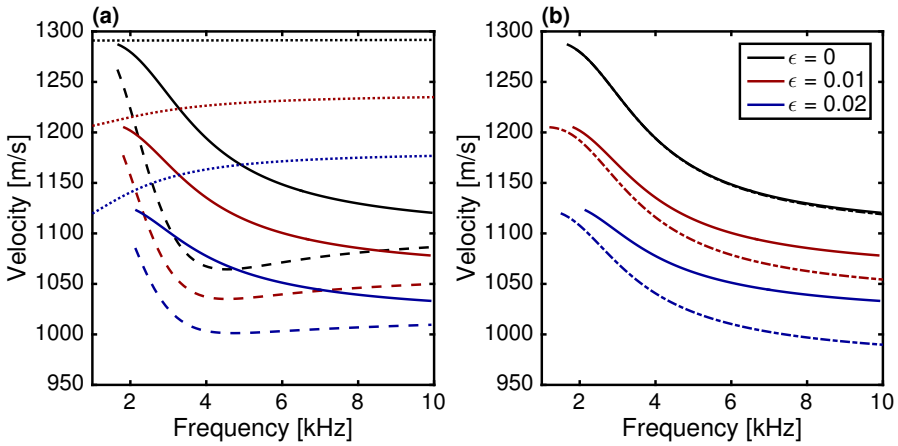

Figure 4.4: (a) Flexural wave phase- (solid lines) and group-velocity (dashed lines) dispersion curves for different crack densities in the slow formation. The effective formation shear-wave velocities for the respective crack density are also displayed (dotted lines). (b) Phase-velocity dispersion comparison using the same low-frequency velocity P- and S-wave velocity limits for the combined squirt- and Biot-flow model (solid lines) and an isotropic elastic model (dashed dot lines).

In a real formation, the critical frequency for squirt-flow dispersion can increase or decrease as, e.g., viscosity, permeability and grain size change. To explore this behavior I use three different values for the time-scale parameter, τ. Changing the time-scale parameter alters the critical frequency at which squirt flow appears. With $\tau = 10^{-3.7}$ s, the squirt-flow critical frequency is below the flexural wave cutoff frequency (see Figure 4.5 black lines), and the predicted velocity would be around the high-frequency squirt-flow velocity limit, below the Biot-flow limit. When $\tau = 10^{-4.3}$ s corresponding to the red lines, the cutoff frequency is around the inflection point of the effective formation S-wave dispersion. The predicted S-wave velocity would most likely be

somewhere in between the low- and high-frequency squirt-flow limits. Lastly, when $\tau = 10^{-4.9}$ s, blue lines, the critical frequency is higher than the low-frequency fluxural-wave cutoff frequency, and the low-frequency limit would be chosen.

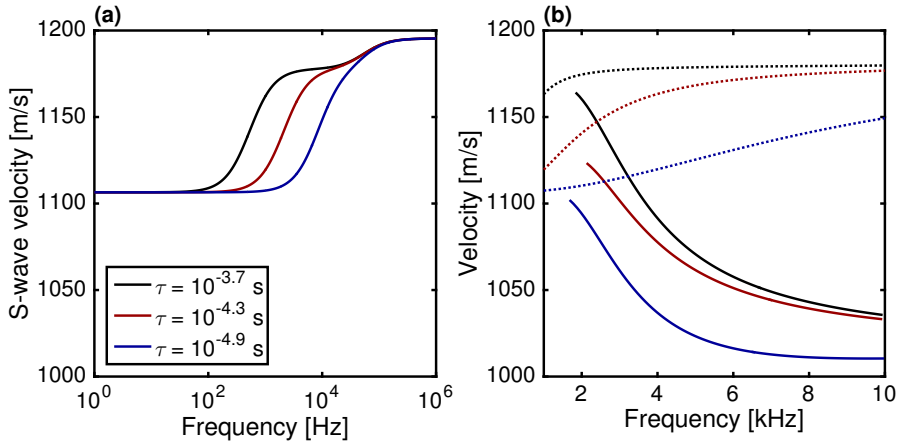

Figure 4.5: (a) Effective formation S-wave velocities for constant crack density corresponding to $\epsilon = 0.02$ for different values of the time-scale parameter τ. (b) Flexural-wave phase-velocity (solid lines) dispersion for the different time-scale parameters together with respective effective S-wave velocities (dotted lines) from Figure a.

4.4.2 Fast formation

The effective formation P- and S-wave velocities in the fast formation (Figure 4.6) show a slight increase in Biot-flow dispersion compared with the slow formation (Figure 4.1) corresponding to $\epsilon = 0$, black lines. With an increase in crack density, I find, as in the slow formation, a decrease in the low-frequency velocity limits together with an increase in effective formation velocity dispersion. In this fast-formation example, Biot- and squirt-flow crit-

ical frequencies are nearly the same.

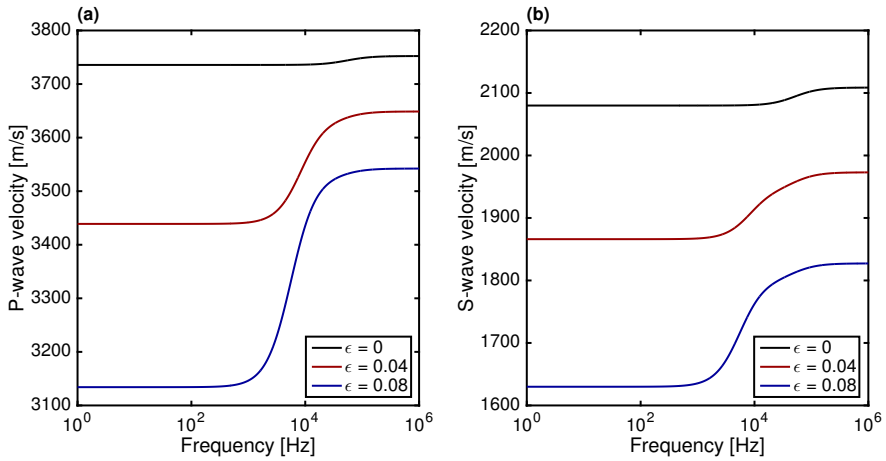

Figure 4.6: Effective formation P- (a) and S-wave (b) velocities in the fast formation (see Table 4.1, fast formation) as a function of increasing crack density. The critical frequency for Biot flow is slightly higher than for squirt flow, but the dispersions appear approximately at the same frequency.

I simulate waveforms using the different crack densities for the fast formation and compare the common-receiver waveforms at $z = 3$ m in Figure 4.7a. Although the shear energy arrives later with an increase in crack density, the Airy phase of the flexural wave tends to arrive earlier with the increase. The moveout for the common–source gather with crack density $\epsilon = 0.04$, is displayed in Figure 4.7b.

I apply WSS on the different 13-receiver shot gathers containing varied crack-density values (Figure 4.8) and overlay the fast effective formation S-wave velocities together with the flexural-dispersion solution of the period equation, white lines. I see that when only Biot flow is present, the effective formation S-wave velocity shows no dispersion over the frequency range con-

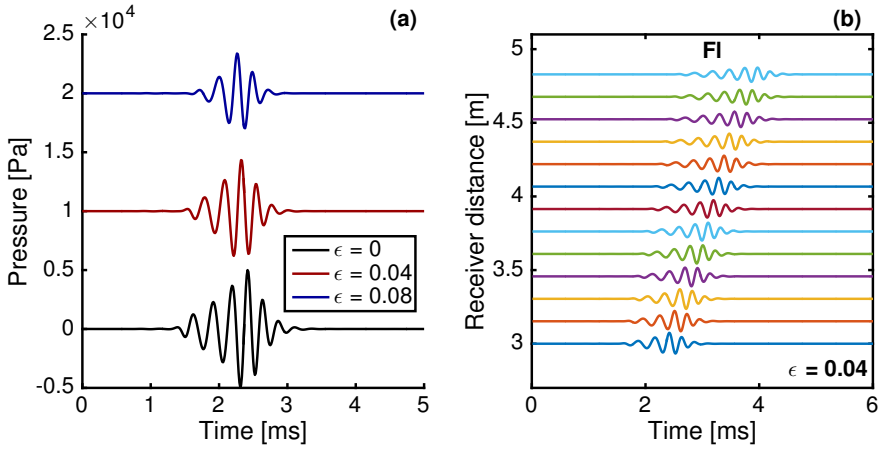

Figure 4.7: (a) Fast formation flexural wave comparison, using a 3-kHz dipole source, for common-receiver waveforms at $z = 3$m, using different crack densities. Although the arrival time for the onset of the flexural wave energy increases with crack density, the arrival time for the Airy phase, related to largest amplitude, is found to decrease. (b) A common-source gather for the formation with crack density of $\epsilon = 0.04$.

sidered. Moreover, in a fast formation a refracted S-wave component of the wavefield exists, which has more energy for lower crack density than for larger and correlates well with the effective formation S-wave velocities. It appears around 8 kHz. However, due to the dispersion of the formation S-wave velocity, the low frequency S-wave prediction from the flexural wave would be lower than the prediction made using a monopole source with a higher frequency excitation.

To illustrate further the crack density effect, I summarize the formation S-wave velocities together with the phase and group velocities of the flexural wave in Figure 4.9. I find the Airy phase of the group velocities increases with crack density, which is in accordance with the observation in Figure 4.7a.

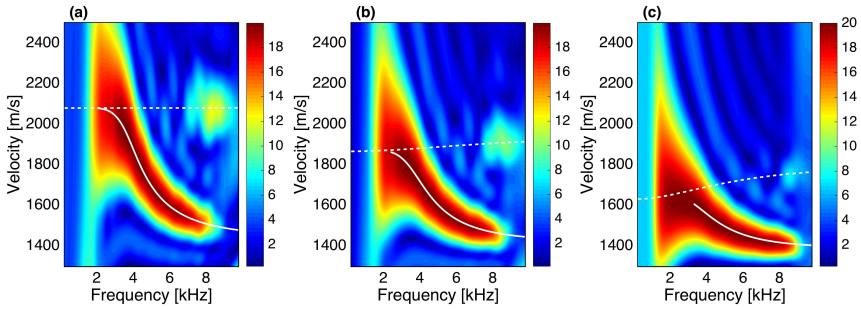

Figure 4.8: WSS dispersion results for the common-source gathers in the fast formation with crack densities $\epsilon = 0$ (a), $\epsilon = 0.04$ (b) and $\epsilon = 0.08$ (c). White dashed lines correspond to the effective S-wave formation velocities from Figure 4.6b and the flexural wave phase velocity dispersion (solid white lines) from solving the period equation. The refracted S-wave velocity is found around 8 kHz. It is lower in terms of semblance but follows the effective formation S-wave velocity.

Similar to the slow formation, I alter the critical squirt-flow frequency by changing the time-scale parameter. In Figure 4.10a I can clearly see the dispersion contribution from squirt and Biot flow, respectively. The flexural wave low-frequency phase-velocity limit increases as the squirt flow critical frequency decreases (Figure 4.10b).

To explore further the sensitivity of the flexural phase-velocity dispersion due to the different parameters affecting/causing the dispersion in the WIFF model, I use Equation 4.13 for the slow and fast formations containing crack densities of 0.02 and 0.04, respectively. I find that for both the slow and fast formations (Figure 4.11), the three parameters that alter the dispersion the most are crack density, porosity and fluid density in the pore space. The flexural-wave phase velocity is relatively insensitive to fluid bulk modulus and

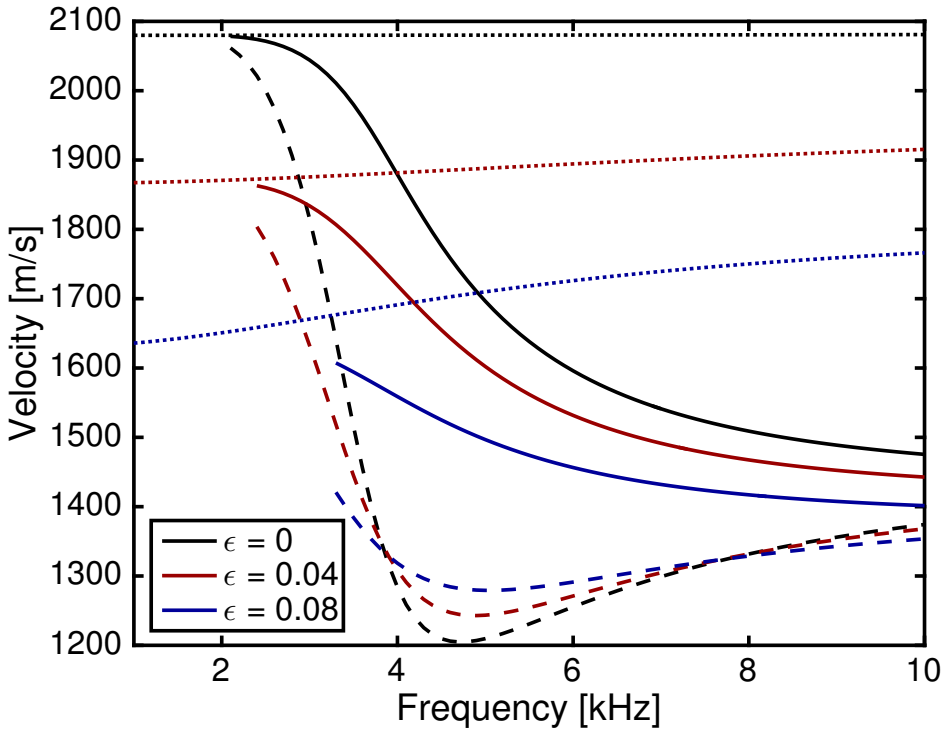

Figure 4.9: Flexural-wave phase- (solid lines) and group-velocity (dashed lines) dispersion using the period equation for different crack densities in the fast formation. The S-wave effective formation velocity from Figure 4.6b is shown as dotted lines.

viscosity. A similar observation is made for the aspect ratio of the compliant pores and permeability of the formation.

4.5 Discussion

My analytical and numerical results show that the presence of compliant pores affects the flexural-wave mode. The waveforms diminish in amplitude, and their phase- and group-velocity dispersion alters. This result is

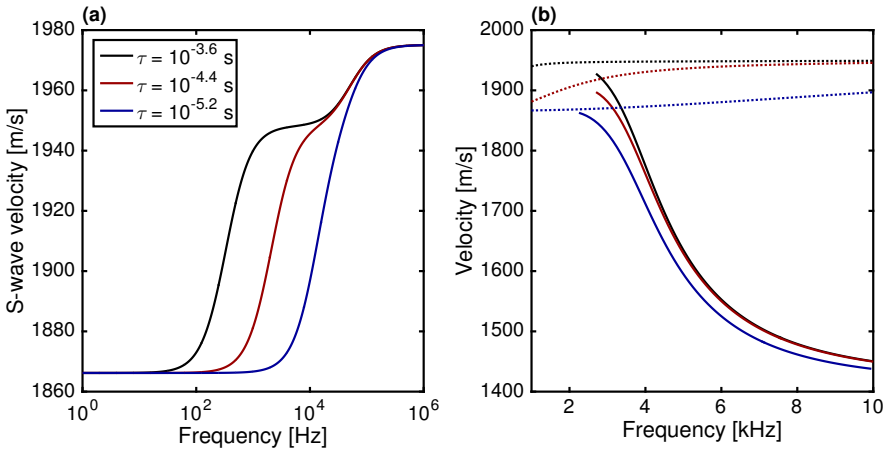

Figure 4.10: (a) Effective S-wave formation velocities in the fast formation for crack density $\epsilon = 0.04$ using different time-scale parameters τ. This changes the location for the critical squirt-flow frequency. (b) Dipole flexural wave phase-velocity dispersion for the different τ values. These are compared with the effective S-wave formation velocities from Figure a.

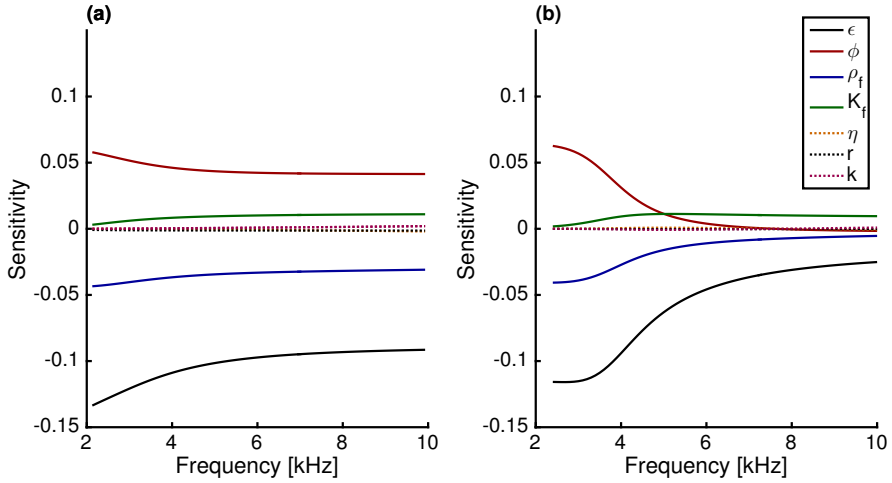

Figure 4.11: Sensitivity for the flexural wave phase velocity using Equation 4.13 in the (a) slow formation with $\epsilon = 0.02$ and (b) fast formation with $\epsilon = 0.04$ as a function of frequency. The parameters tested all contribute to the WIFF dispersion.

in agreement both from processing the waveforms with WSS and by solving the period equation. In the slow formation with compliant pores, the critical squirt-flow frequency is around 500 Hz, with the high-velocity frequency limit reached around 4 kHz (Figure 4.3c). For the fast formation with compliant pores, the critical frequency and the high-frequency limit is around 2 kHz and 8 kHz, respectively (Figure 4.8). In both the slow and fast formations, the flexural wave reaches its low-frequency phase-velocity limit around 2 kHz, which is also from where I would ideally predict the S-wave velocity. Due to the lower critical frequency in the slow formation, the S-wave velocity prediction from the flexural wave would thus be slightly faster than the velocity traveled by the seismic waves at lower frequencies. For the fast formation with compliant pores, monopole and dipole S-wave predictions would be different, with the dipole shear predicting a lower velocity than the monopole shear. I illustrate further this velocity prediction ambiguity by changing where the critical squirt-flow frequency occurs (figures 4.5 and 4.10).

The parameters crack density, porosity and fluid density are all significant contributors to the change in formation S-wave velocities. Similar to Sinha (1997), I find the flexural-wave phase velocity in the slow formation to be sensitive to the S-wave velocity changes throughout the entire dipole bandwidth. In the fast formation, the sensitivity occurs around $2 - 4$ kHz. Thus, a model-based inversion might work better in the fast formation than in the slow. However, Figure 4.4b shows that using a simple elastic model-based inversion would most likely give erroneous S-wave predictions in a formation

where compliant pores cause dispersion around the dipole frequency bandwidth. Thus, care should be taken to understand the dispersion behavior before correcting for the flexural-wave dispersion so that the correct model is used in the inversion.

4.6 Conclusions

This work presented a theoretical and numerical study of the flexural wave mode generated by a dipole source in a fluid-filled borehole surrounded by a fluid-saturated dual porosity medium subject to both squirt and Biot flow. The purpose of this study was to understand the extent to which we might trust the dipole shear velocity when fluid-saturated compliant pores are present and any additional effects that could be used for reservoir characterization and other related purposes. The numerical modeling demonstrates the effective formation P- and S-wave velocities to be significantly affected by the presence of compliant pores, which in turn lowers the low-frequency limit of the flexural-wave phase velocity in addition to altering the dispersion behavior. Depending on where the critical squirt-flow frequency appears, various dipole shear velocities could be estimated, bounded by the high- and low-frequency limit of the effective formation shear wave velocity. Furthermore, computational results from the sensitivity analyses indicate the flexural wave to be primarily sensitive to compliant pores in a slow formations. In the fast formation, the sensitivity to compliant pores of the flexural-wave phase velocity decreases with higher frequency.

Chapter 5

Conclusions and future work

5.1 Conclusions

The main objective of this dissertation was to provide a more complete understanding of how borehole acoustic waveforms interact with rock-formations containing fluid-filled heterogeneous pore space. This larger goal was subdivided into two parts. The first step involved developing a frequency-dependent wave equation that could accurately describe the effect of local and global flow dispersion mechanisms. The second step was to numerically simulate waveforms in boreholes surrounded by formations subject to local and global flow.

In chapter 2, I demonstrated using Chapman's squirt-flow formulism how to derive modified dry-frame moduli containing fluid-saturated compliant pores. The derived modified-frame moduli were incorporated in Gassmann's or Biot's theory to estimate either the effect of squirt flow or the combined effect of squirt and Biot flow over a wide range of frequencies. The benefit of combining the modified frame with Gassmann's over using the full theory of Chapman is the flexibility the combined theory has in choosing the dry moduli while still being consistent with the full theory of Chapman. When comparing

Chapman's model with Gurevich et al. (2010) and Mavko and Jizba (1991) squirt-flow models, I find the theories main differences to be the two input parameters, μ and K_h. The parameter μ corresponds to shear mineral moduli, which is used Chapman's theory alone. The second parameter, K_h, is the dry moduli without compliant pores, which is used in Gurevich et al. (2010) and Mavko and Jizba (1991) models, but not in Chapman's theory. I tested the prediction of my Biot-Chapman theory, using the dry measured velocities as a function of pressure, against fluid-saturated ultrasonic measurements and compared them with Gassmann, Biot and Mavko-Jizba fluid-saturated theories. I found my theory to perform slightly better then all others. One of the reasons is the difficulty in estimating K_h, used in Mavko-Jizba's theory, which is estimated from the high-pressure ultrasonic measurements. I believe it to be unlikely that the stiff pore-space is completely unaffected by the higher pressures.

In chapter 3, I applied the unified Biot-Chapman theory from Chapter 2 to a slow and fast formation to study the effect of fluid-saturated compliant pores on acoustic wave-forms generated with a monopole source. The modeling results show compliant pores to have a substantial effect on both the P- and S-wave modes in both slow and fast formations. The compliant pores lower the velocities and cause increasing phase velocity dispersion. I also find the phase-velocity dispersion and amplitude of the Stoneley wave mode to be significantly affected by compliant pores. The sensitivity is mostly due to velocity alterations in formation P- and S-wave velocities and not due to changes

in fluid-flow mobility.

Chapter 4 presented waveforms generated with a dipole source in a fluid-filled borehole surrounded by a formation containing stiff and compliant pores, using the unified Biot-Chapman theory derived in Chapter 2. I study both a slow and fast formation similar to the ones investigated in Chapter 3. I find the fluid-saturated compliant pores to significantly affect the flexural wave in both phase- and group-velocity dispersion. The compliant pores lower the low-frequency velocity limit of the flexural wave and decrease the amplitude. I also find that out of all the parameters influencing WIFF, the compliant pores are the main contributors to changes in the velocity dispersion.

The main contributions of this dissertation include unifying Biot's wave-equation with Chapman's squirt flow model. This model accounts for the heterogeneous pores space of the rock that results in local- and global-flow. The model was used to understand the complex interaction between fluid and solid in acoustic wave propagation. Most of the previous studies on borehole acoustic waveforms only account for global flow, where only the Stoneley wave is truly affected. Integrating the small-scale pore-space features through Chapman's theory revealed significant influence of local flow on all of the wave modes.

5.2 Limitations

This dissertation provides a wave equation that accounts for local and global flow. As with any mathematical model attempting to explain physi-

cal and observable phenomena, limitations apply. Certain parameters in the combined Biot-Chapman's model are relatively easy to constrain through laboratory measurements, such as total porosity, permeability and density of the rock sample together with the fluid properties, fluid density, compressibility and viscosity. Two parameters, crack aspect ratio and the amount of compliant porosity, on the other hand, are extremely difficult to constrain. Although crack aspect ratio has a well defined meaning mathematically, no true pore-space is a perfect ellipsoid, and the parameter is, therefore, used more as a fitting parameter for specific measurements. This is a notable limitation on the predictability of the combined theory, but it is difficult to overcome when adding local flow to any theory. Compliant porosity is often times estimated from variation of total porosity as a function of pressure. However, considering that compliant porosity is usually less then 0.1%, extremely accurate total porosity measurements are needed. If they do not exist, then the errors in this parameter might lead to erroneous velocity dispersion estimates.

Furthermore, in the following model squirt flow is assumed to give rise to frequency dependent moduli, which are incorporated separately in Biot's poroelastic theory. This assumption could pose a problem in the dispersion estimates because Biot and squirt flow are in reality caused by the same fluid flow. However, physical theories always have a trade off between simplicity/user friendliness versus complexity/more correct estimations.

The combined Biot squirt-flow theory is applicable for isotropic formations only where the direction of the compliant ellipsoidal microcracks are

assumed uniformly distributed. In the subsurface, directional stresses exist due to, i.e., overburden, faults and tectonic movement. This will cause the quantity of open compliant pores to be directional dependent and ultimately cause an isotropic rock to become anisotropic. This could possibly be addressed by assuming a nonuniform distribution of normal crack direction in the derivation of the modified frame moduli.

The use of the derived WIFF wave equation on borehole sonic measurements is limited to isotropic formations containing Biot and squrt flow, with a axisymmetric borehole containing a permeable borehole wall. No tool response is assumed. These assumptions make the applicability of the results limited, especially because in reality the wave modes will also be affected by complexities and irregularities such as borehole mud invasion, rugosity, dipping layers and anisotropy. All these parameters affect the wave modes to various degrees and might make the effect of the WIFF mechanisms negligible.

In spite of these limitations, theoretical understanding of simpler systems, such as this model, can provide us with insight into more complex system behavior and is thus still of significant importance.

5.3 Future work

In this dissertation, I simulated acoustic waveforms using the discrete summation method, where the source is centralized in the fluid-filled borehole together with the receivers. The surrounding formation is considered perfectly vertical and reaches out to infinity in the radial direction. Although this

approach is valuable for understanding the effect of isolated compliant pores on wavemodes, it is restricted to limitations and assumptions of the theory, and therefore, might give unrealistic results for what compliant pores actually do to the different wave modes in more complex borehole scenarios. I think a very good direction for future research would be to include more complex borehole settings, i.e., including the tool response, layering effects and borehole rugosity. This could lead to an understanding as to what extent we can decipher the presence of compliant pores from the acoustic waveforms.

Appendices

Appendix A

Squirt flow coefficients

The frequency-dependent coefficients used in Chapman's theory are given by,

$$C_1(\omega) = \frac{1}{1+i\omega\tau}\left(\frac{i\omega\tau}{1+K_c} + (1+i\omega\tau\gamma)B_1(\omega)\right), \tag{A.1}$$

and

$$C_2(\omega) = \frac{1}{1+i\omega\tau}\left(-\gamma' i\omega\tau + (1+i\omega\tau\gamma)B_2(\omega)\right), \tag{A.2}$$

where

$$B_1(\omega) = \frac{l}{(l-l\gamma+\gamma+i\omega\tau\gamma)}\frac{1}{(1+K_c)}, \tag{A.3}$$

$$B_2(\omega) = \frac{1}{l-l\gamma+\gamma+i\omega\tau\gamma}\gamma'(1-l+i\omega\tau). \tag{A.4}$$

The terms γ and γ' are given by,

$$\gamma = \frac{3\sigma_c(1+K_p)}{4\mu_m r(1+K_c)} \tag{A.5}$$

and

$$\gamma' = \gamma\frac{(1-\nu)}{(1+\nu)}\frac{1}{1+K_p}. \tag{A.6}$$

The timescale parameter τ which determines at which frequencies the squirt flow takes place is given by,

$$\tau = \frac{\eta c_v(1+K_c)}{6k\zeta\sigma_c}, \tag{A.7}$$

where η is the viscosity of the fluid, $c_v = 4\pi a^3 r/3$ is the crack volume, a denoting the crack radius, k is the permeability and ζ is the grain size. This parameter which decides at which frequencies the squirt flow is apparent was mentioned by (Chapman, 2001) to be the most difficult parameter to estimate and will for me be a rough estimate. I also have l corresponding to the fraction of cracks in the pore space,

$$l = \frac{N_c}{N} = \frac{\frac{4}{3}\pi\epsilon}{\frac{4}{3}\pi\epsilon + \phi_p}, \tag{A.8}$$

where $\epsilon = 3\phi_c/(4\pi r)$ is the crack density.

The full expression for the bulk and shear moduli in the theory of Chapman et al. (2002) containing spherical pores and oblate spheroids with small aspect ratios is given by,

$$K_{eff}(\omega) = K_{dry} + \phi_c(\frac{K_m^2}{\sigma_c} + K_m)(C_1(\omega) + 3C_2(\omega)) + \phi_p(\frac{3}{4}\frac{K_m^2}{\mu_m} + K_m)(B_1(\omega) + 3B_2(\omega)), \tag{A.9}$$

and

$$\mu_{eff}(\omega) = \mu_{dry} + \phi_c \frac{4\mu_m^2 C_1(\omega)}{15\sigma_c}, \tag{A.10}$$

where K_{dry} and μ_{dry} are explicitly given by Equations 2.3 and 2.4.

Appendix B

Biot+squirt flow

The solutions to the wave equation in Biot (1956a) in the form of the fast P- and S-wave phase velocities are given by,

$$V_p(\omega) = \omega/k_p(\omega) \tag{B.1}$$

and

$$V_s(\omega) = \omega/k_s(\omega), \tag{B.2}$$

where

$$k_p^2 = \frac{N - \sqrt{N^2 - 4MO}}{2M} \tag{B.3}$$

and

$$k_s^2 = \frac{O}{\mu(\rho_{22}\omega^2 + i\omega b)}. \tag{B.4}$$

The expressions for M, N, O are given by

$$M = (A + 2\mu)R - Q^2, \tag{B.5}$$

$$N = i\omega b(A + 2\mu + 2Q + R) + \omega^2(\rho_{11}R + \rho_{22}(A + 2\mu) - 2\rho_{12}Q), \tag{B.6}$$

$$O = \omega^2(i\omega\rho b + \omega^2(\rho_{11}\rho_{22} - \rho_{12}^2)). \tag{B.7}$$

while the coefficients A, μ, Q and R are

$$A = \frac{(1-\phi)(1-\phi-\frac{K_b(\omega)}{K_m})K_m + \phi\frac{K_m}{K_f}K_b(\omega)}{1-\phi-\frac{K_b(\omega)}{K_m} + \phi\frac{K_m}{K_f}} - \frac{2}{3}\mu_b(\omega), \tag{B.8}$$

$$\mu = \mu_b(\omega), \tag{B.9}$$

$$Q = \frac{(1-\phi-\frac{K_b(\omega)}{K_m})\phi K_m}{1-\phi-\frac{K_b(\omega)}{K_m}+\phi\frac{K_m}{K_f}}, \tag{B.10}$$

$$R = \frac{\phi^2 K_m}{1-\phi-\frac{K_b(\omega)}{K_m}+\phi\frac{K_m}{K_f}}. \tag{B.11}$$

In the above equations $\rho_{11} = (1-\phi)\rho_m - (1-\alpha)\phi\rho_f$, $\rho_{22} = \alpha\phi\rho_f$ and $\rho_{12} = (1-\alpha)\phi\rho_f$, where ϕ denotes the total porosity, ρ_m and ρ_f are the mineral and fluid densities, respectively, α is the tortuosity, a purely geometric factor, and the parameter $b = \eta\phi^2/k$ (Plona and Johnson, 1980; Mavko et al., 2009). The parameters $K_b(\omega)$ and $\mu_b(\omega)$ denotes the dry modified frame from the various theories. To estimate only the Biot dispersion I set $K_b(\omega) = K_{dry}$ and $\mu_b(\omega) = \mu_{dry}$. Note that for the expressions for Mavko and Jizba (1991) modified frame, Equations 2.14 and 2.15 there is no frequency dependence.

Appendix C

Synthetic microseismograms in poroelastic media containing cracks and pores

To simulate waveforms in axisymmetric boreholes with no tool embedded in Biot's poroelastic formation containing squirt-flow dissipation and a permeable interface, I use the discrete wavenumber summation method (Cheng and Toksöz, 1981; Tang and Cheng, 2004). The result for a monopole in terms of pressure is,

$$P(z,t) = \int_{-\infty}^{\infty} S(\omega) D_o(\omega) e^{-i\omega t} d\omega + \int_{-\infty}^{\infty}\int_{-\infty}^{\infty} S(\omega) \tilde{A}_{fl}^{(0)}(k_z,\omega) e^{ik_z z} e^{-i\omega t} dk_z d\omega \tag{C.1}$$

And for a multipole of nth order the result is

$$\begin{aligned} M_n(z,t) = &\int_{-\infty}^{\infty} S(\omega) D_n(\omega) e^{-i\omega t} d\omega + \\ &+ \frac{r_0^n}{2^{2n} n!} \int_{-\infty}^{\infty}\int_{-\infty}^{\infty} k_r^{(fl)2n} S(\omega) \tilde{A}_{fl}^{(n)}(k_z,\omega) e^{ik_z z} e^{-i\omega t} dk_z d\omega, \end{aligned} \tag{C.2}$$

where $S(\omega)$ denotes the source spectrum. A Ricker wavelet is often used.

$$S(\omega) = (\frac{\omega}{\omega_0})^2 e^{(-\omega/\omega_0)^2}. \tag{C.3}$$

$D_n(\omega)$ the contribution coming directly from the source radiation.

$$D_n(\omega) = \frac{\pi \varepsilon_n r_0^n}{2^{2n} n!} \sum_{m=0}^{n} C_m^n (-2ik_{fl})^m \frac{(2n-m)!}{z^{2n-m+1}} e^{ik_{fl} z} \tag{C.4}$$

The reason for the change of symbol $M_n(z,t)$ instead of $P(z,t)$ in Eq. C.2 is due to the fact that for a dipole what is measured is not pressure but displacement, and for a quadrupole source the spatial derivative of displacement is measured and so on.

The term $\tilde{A}_{fl}^{(n)}(k_z,\omega)$ denotes the refracted and reflected wavefields in the borehole. This variable is found by first solving the wave equation in the borehole fluid and formation separately. Employing boundary conditions at the permeable borehole wall allows me to couple the two solutions. The boundary conditions used are the same as in Schmitt (1988d), which are a balance of fluid volume flux, continuity of radial stress, zero azimuthal and tangential stresses in the solid and equal fluid pressure at the borehole wall. From these conditions I arrive at

$$\mathbf{M}\bar{\mathbf{x}} = \bar{\mathbf{b}}, \tag{C.5}$$

where the matrix $\mathbf{M}$ and the vector $\bar{\mathbf{b}}$ are given below and $\bar{\mathbf{x}} = [\tilde{A}_{fl}^{(n)}, \tilde{A}_{f}^{(n)}, \tilde{A}_{s}^{(n)}, \tilde{B}^{(n)}, \tilde{C}^{(n)}]^{\mathrm{T}}$ setting n=0 for a monopole source and n=1 for a dipole source. The coefficients $\tilde{A}_{f}^{(n)}, \tilde{A}_{s}^{(n)}$ describe the fast and slow compressional waves, and $\tilde{B}^{(n)}, \tilde{C}^{(n)}$ the SH and the SV-type shear waves in the formation containing Biot and squirt flow.

From Equation C.5 I can solve for $\tilde{A}_{fl}^{(n)}(k_z,\omega)$. The integrals in Equation C.1 can be calculated using the wavenumber summation method (Cheng and Toksöz, 1981) and a fast Fourier transform.

$$M_{11} = k_r^{(fl)} I_{n+1}(k_r^{(fl)} R) + \frac{n}{R} I_n(k_r^{(fl)} R)$$
$$M_{12} = (k_r^{(f)} K_{n+1}(k_r^{(f)} R) - \frac{n}{R} K_n(k_r^{(f)} R))(1 + \phi(\mu_f - 1))$$
$$M_{13} = (k_r^{(s)} K_{n+1}(k_r^{(s)} R) - \frac{n}{R} K_n(k_r^{(s)} R))(1 + \phi(\mu_s - 1))$$
$$M_{14} = -\frac{n}{R} K_n(k_r^{(t)} R)(1 + \phi(\alpha_0 - 1))$$
$$M_{15} = ik_z(k_r^{(t)} K_{n+1}(k_r^{(t)} R) - \frac{n}{R} K_n(k_r^{(t)} R))(1 + \phi(\alpha_0 - 1))$$

$$M_{21} = -\rho_{fl}\omega^2 I_n(k_r^{(fl)} R)$$
$$M_{22} = -2\mu\Big(K_n(k_r^{(f)} R)\Big(k_r^{(f)2} + \frac{n(n-1)}{R^2}\Big) + \frac{k_r^{(f)}}{R} K_{n+1}(k_r^{(f)} R)\Big) +$$
$$k_f^2 K_n(k_r^{(f)} R)\Big(A + Q + \mu_f(Q + R_{biot})\Big)$$
$$M_{23} = -2\mu\Big(K_n(k_r^{(s)} R)\Big(k_r^{(s)2} + \frac{n(n-1)}{R^2}\Big) + \frac{k_r^{(s)}}{R} K_{n+1}(k_r^{(s)} R)\Big) +$$
$$k_s^2 K_n(k_r^{(s)} R)\Big(A + Q + \mu_s(Q + R_{biot})\Big)$$
$$M_{24} = -2\mu\Big(\frac{n}{R^2}(n-1)K_n(k_r^{(t)} R) - \frac{n}{R} k_r^{(t)} K_{n+1}(k_r^{(t)} R)\Big)$$
$$M_{25} = -2\mu i k_z\Big(\big(\frac{n}{R^2}(n-1) + k_r^{(t)2}\big)K_n(k_r^{(t)} R) + \frac{k_r^{(t)}}{R} K_{n+1}(k_r^{(t)} R)\Big)$$

$$M_{31} = 0$$
$$M_{32} = -2\mu\Big(\frac{n}{R^2}(n-1)K_n(k_r^{(f)} R) - \frac{n k_r^{(f)}}{R} K_{n+1}(k_r^{(f)} R)\Big)$$
$$M_{33} = -2\mu\Big(\frac{n}{R^2}(n-1)K_n(k_r^{(s)} R) - \frac{n k_r^{(s)}}{R} K_{n+1}(k_r^{(s)} R)\Big)$$
$$M_{34} = -\mu\Big(K_n(k_r^{(t)} R)\big(\frac{2n}{R^2}(n-1) + k_r^{(t)2}\big) + K_{n+1}(k_r^{(t)} R)\frac{2k_r^{(t)}}{R}\Big)$$
$$M_{35} = -2\mu i k_z\Big(K_n(k_r^{(t)} R)\big(\frac{n}{R^2}(n-1)\big) - \frac{n k_r^{(t)}}{R} K_{n+1}(k_r^{(t)} R)\Big)$$

$$M_{41} = 0$$

$$M_{42} = 2\mu i k_z \Big(\frac{n}{R} K_n(k_r^{(f)} R) - k_r^{(f)} K_{n+1}(k_r^{(f)} R) \Big)$$

$$M_{43} = 2\mu i k_z \Big(\frac{n}{R} K_n(k_r^{(s)} R) - k_r^{(s)} K_{n+1}(k_r^{(s)} R) \Big)$$

$$M_{44} = \frac{\mu n i k_z}{R} K_n(k_r^{(t)} R)$$

$$M_{45} = \mu \big(k_t^2 - 2k_z^2 \big) \Big(\frac{n}{R} K_n(k_r^{(t)} R) - k_r^{(t)} K_{n+1}(k_r^{(t)} R) \Big)$$

$$M_{51} = -\rho_{fl} \omega^2 I_n(k_r^{(fl)} R)$$

$$M_{52} = \frac{\big(Q + \mu_f R_{biot} \big) k_f^2}{\phi} K_n(k_r^{(f)} R)$$

$$M_{53} = \frac{\big(Q + \mu_s R_{biot} \big) k_s^2}{\phi} K_n(k_r^{(s)} R)$$

$$M_{54} = 0$$

$$M_{55} = 0$$

$$b_1 = -\varepsilon_n (-k_r^{(fl)} K_{n+1}(k_r^{(fl)} R) + \frac{n}{R} K_n(k_r^{(fl)} R))$$

$$b_2 = \varepsilon_n \rho_{fl} \omega^2 K_n(k_r^{(fl)} R)$$

$$b_3 = 0$$

$$b_4 = 0$$

$$b_5 = \varepsilon_n \rho_{fl} \omega^2 K_n(k_r^{(fl)} R)$$

In the system of equations above, I_n and K_n, corresponds to the modified Bessel functions of the first and second kind and of order n, n and ε_n is set to 0 for a monopole source and 1 for a dipole source. The radial wavenumber in the borehole-fluid is, $k_r^{(fl)2} = k_z^2 - (\omega/V_{fl})^2$, where k_z is the axial wavenumber, V_{fl} the borehole fluid velocity and ω the angular frequency. The radial wavenumbers in the formation is given by $k_r^{(i)2} = k_z^2 - k_i^2$, with $i = [f, s, t]$, while R is the borehole radius. The complex wavenumbers, $k_{f,s}$, for the fast and slow P-wave, respectively, and k_t which is the wavenumber for the S-wave are given by

$$k_{f,s}^2 = \frac{N \mp \sqrt{N^2 - 4MO}}{2M} \tag{C.6}$$

and

$$k_t^2 = \frac{O}{\mu(\rho_{22}\omega^2 + j\omega b)} \tag{C.7}$$

where

$$M = (A + 2\mu)R_{biot} - Q^2, \tag{C.8}$$

$$N = \omega^2(\rho_{11}R_{biot} + \rho_{22}(A + 2\mu) - 2\rho_{12}Q) + j\omega b(A + 2\mu + 2Q + R_{biot}), \tag{C.9}$$

$$O = \omega^2(\omega^2(\rho_{11}\rho_{22} - \rho_{12}^2) + j\omega\rho b), \tag{C.10}$$

and

$$\mu_{f,s} = \frac{\omega^2(\rho_{11}R_{biot} - \rho_{12}Q) - k_{f,s}^2((A + 2\mu)R_{biot} - Q^2) + j\omega b(Q + R_{biot})}{\omega^2(\rho_{22}Q - \rho_{12}R_{biot}) + j\omega b(Q + R_{biot})} \tag{C.11}$$

together with

$$\alpha_0 = -\frac{\omega^2\rho_{12} - j\omega b}{\omega^2\rho_{22} + j\omega b}. \tag{C.12}$$

The expressions for A, μ, Q and R_{biot} are given by,

$$A = \frac{(1-\phi)(1-\phi-\frac{K_b(\omega)}{K_m})K_m + \phi\frac{K_m}{K_f}K_b(\omega)}{1-\phi-\frac{K_b(\omega)}{K_m}+\phi\frac{K_m}{K_f}} - \frac{2}{3}\mu_b(\omega), \tag{C.13}$$

$$\mu = \mu_b(\omega), \tag{C.14}$$

$$Q = \frac{(1-\phi-\frac{K_b(\omega)}{K_m})\phi K_m}{1-\phi-\frac{K_b(\omega)}{K_m}+\phi\frac{K_m}{K_f}}, \tag{C.15}$$

$$R_{biot} = \frac{\phi^2 K_m}{1-\phi-\frac{K_b(\omega)}{K_m}+\phi\frac{K_m}{K_f}}. \tag{C.16}$$

Bibliography

L. Baron and K. Holliger. Analysis of the velocity dispersion and attenuation behavior of multifrequency sonic logs. In R. Miller, J. Bradford, and K. Holliger, editors, *Advances in Near-Surface Seismology and Ground-Penetrating Radar*, chapter 9, pages 153–166. Society of Exploration Geophysicists, 2010.

M. A. Biot. Theory of propagation of elastic waves in a fluid-saturated porous solid. i. low-frequency range. *Journal of the Acoustical Society of America*, 28:168–176, 1956a.

M. A. Biot. Theory of propagation of elastic waves in a fluid-saturated porous solid. ii. higher frequency range. *Journal of the Acoustical Society of America*, 28:179–191, 1956b.

M. A. Biot. The elastic coefficients of the theory of consolidation. *Journal of Applied Mechanics*, 24:594–601, 1957.

M. A. Biot. Mechanics of deformation and acoustic propagation in porous media. *Journal of the Acoustical Society of America*, 33:1482–1498, 1962a.

M. A. Biot. Generalized theory of acoustic propagation in porous dissipative media. *Journal of the Acoustical Society of America*, 34:1254–1264, 1962b.

J. M. Carcione. *Wave fields in real media: Theory and numerical simulation*

of wave propagation in anisotropic, anelastic, porous and electromagnetic media. Elsevier Scientific Publ. Co. Inc., 3 edition, 2014.

M. E. Chapman. *Modeling the wide-band laboratory response of rock samples to fluid and pressure changes*. PhD thesis, University of Edinburgh, 2001.

M. E. Chapman. Frequency-dependent anisotropy due to meso-scale fractures in the presence if equant porosity. *Geophysical Prospecting*, 51:369–379, 2003.

M. E. Chapman, S. V. Zatsepin, and S. Crampin. Derivation of a microstructural poroelastic model. *Geophysical Journal International*, 151:427–451, 2002.

X. Chen, X. Tang, and Y. Qian. Simulation of multipole acoustic logging in cracked porous formations. *Geophysics*, 79(1):D1–D10, 2014.

C. H. Cheng and M. N. Toksöz. Elastic wave propagation in a fluid-filled borehole and synthetic acoustic logs. *Geophysics*, 46(7):1042–1053, 1981.

C. H. Cheng, Z. Jinzhong, and D. R. Burns. Effects of in-situ permeability on the propagation of stoneley (tube) waves in a borehole. *Geophysics*, 52(9): 1279–1289, 1987.

N. P. Chotiros and M. J. Isakson. A broadband model of sandy ocean sediments: Biot-stoll with contact squirt flow and shear drag. *The Journal of the Acoustical Society of America*, 116(4):2011–2022, 2004.

K. B. Coyner. *Effects od stress, pore pressure, and pore fluids on bulk strain, velocity, and permeabillity in rocks*. PhD thesis, University of Arizona, 1977.

E. J. H. Dahl and K. T. Spikes. Local and global fluid effects on sonic wave modes. *Geophysics*, 58(4):524–533, 2017.

J. Dvorkin and A. Nur. Dynamic poroelasticity: A unified model with the squirt and the biot mechanisms. *Geophysics*, 58(4):524–533, 1993.

J. Dvorkin, R. Nolen-Hoeksema, and A. Nur. The squirt-flow mechanism: Macroscopic description. *Geophysics*, 59(3):428–438, 1994.

J. D. Eshelby. The determination of the elastic field of an ellipsoidal inclusion, and related problems. *Proceedings of the Royal Society of London A*, 241: 376–396, 1957.

F. Gassmann. Über die elastizität poröser medien. *Vierteljahrsschrift der Naturforschenden Gesselschaft in Zurich*, 96:1–23, 1951.

T. W. Geeritz and X. Tang. Centroid phase slowness as a tool for dispersion correction of dipole acoistic logging data. *Geophysics*, 68(1):101–107, 2003.

B. Gurevich, D. Makarynska, O. B. De Paula, and M. Pervukhina. A simple model for squirt-flow dispersion and attenuation in fluid-saturated granular rocks. *Geophysics*, 75(6):109–120, 2010.

X. He, H. Hu, and W. Guan. Fast and slow flexural waves in a deviated borehole in homogeneous and layered anisotropic formations. *Geophysical Journal International*, 181:417–426, 2010.

X. He, H. Hu, and X. Wang. Finite difference modelling of dipole acoustic logs in a poroelastic formation with anisotropic permeability. *Geophysical Journal International*, 192:359–374, 2013.

X. Huang and H. Yin. A data-driven approach to extract shear and compressional slowness from dispersive waveform data. 75th Annual International Meeting, SEG, Expanded Abstract, 2005.

D. J. Keller. Acoustic wave propagation in composite fluid saturated media. *Geophysics*, 54:1554–1563, 1989.

W. K. Kenneth, H. Liu, and D. L. Johnson. Permeability and borehole stoneley waves: Comparison between experiment and theory. *Geophysics*, 54:66–75, 1989.

C. V. Kimball. Shear slowness measurement by dispersive processing of the borehole flexural mode. *Geophysics*, 63:337–344, 1998.

C. V. Kimball and T. L. Marzetta. Semblance processing of borehole acoustic array data. *Geophysics*, 49:274–281, 1986.

A. L. Kurkjian and S. Chang. Acoustic multipole sources in fluid-filled boreholes. *Geophysics*, 51(1):148–163, 1986.

S. Lee, X. Tang, Y. Su, and C. Zhuang. Dispersion correction of borehole dipole shear data to enhance reservoir fluid characterization. 86th Annual International Meeting, SEG, Expanded Abstract, 2016.

H. D. Leslie and C. J. Randall. Mutlipole sources in boreholes penetrating anisotropic formations: Numerical and experimental results. *Journal of Acoustical Society of America*, 91:12–27, 1992.

Q. Liu and B. K. Sinha. Multipole acoustic waveforms in fluid-filled boreholes in biaxially stressed formations: A finite-difference method. *Geophysics*, 65 (1):190–201, 2000.

Q. Liu and B. K. Sinha. A 3d cylindrical pml/fdtd method for elastic waves in fluid-filled pressurized boreholes in triaxially stressed formations. *Geophysics*, 68(1):1731–1743, 2003.

J. Ma, P. J. Matuszyk, R. K. Mallan, C. Torres-Verdin, and B. C. Voss. Joint processing of forward and backward extended prony and weighted spectral semblance methods for robust extraction of velocity dispersion data. Proceedings of The Society of Petrophysicists and Well Log Analysts (SPWLA) Meeting, Perth, Australia, 6 2010.

R. K. Mallan, C. Torres-Verdin, and J. Ma. Simulation of borehole sonic waveforms in dipping, anisotropic, and invaded formations. *Geophysics*, 76 (4):E127–E139, 2011.

I. Markova, G. Ronquillo Jarillo, M. Markov, and B. Gurevich. Squirt flow influence on sonic log parameters. *Geophysical Journal International*, 196: 1082–1091, 2014.

G. Mavko and D. Jizba. Estimating grain-scale fluid effects on velocity dispersion in rocks. *Geophysics*, 56:1940–1949, 1991.

G. Mavko and A. Nur. Melt squirt in the asthenosphere. *Journal of Geophysical Research*, 80:1444–1448, 1975.

G. Mavko, T. Mukeriji, and J. Dvorkin. *The rock physics handbook: tools for seismic analysis of porous media*. Cambridge University Press, 2 edition, 2009.

T. M. Müller, B. Gurevich, and M. Lebedev. Seismic wave attenuation and dispersion resulting from wave-induced flow in porous rocks a review. *Geophysics*, 75:75A147–75A164, 2010.

W. F. Murphy, K. W. Winkler, and R. L. Kleinberg. Acoustic relaxation in sedimentary rocks: Dependence on grain contacts and fluid saturation. *Geophysics*, 51:757–766, 1986.

B. Nolte and X. J. Huang. Dispersion analysis of split flexural waves. Annual report of borehole acoustics and logging and reservoir delineation consortia, Massachusetts Institute of Technology, 1997.

R. J. O'Connell and B. Budiansky. Viscoelastic properties of fluid-saturated cracked solids. *Journal of Geophysical Research*, 82:5719–5735, 1977.

P. R. Ogushwitz. Applicability of the biot theory. i. low-porosity material. *Journal of Acoustical Society of America*, 77:429–440, 1985.

J. D. Palmer and M. L. Traviola. Attenuation by squirt flow in undersaturated gas sands. *Geophysics*, 45:1780–1792, 1980.

D. Pardo, P. J. Matuszyk, C. Torres-Verdin, A. Mora, I. Muga, and V. M. Calo. Influence of borehole-eccentred tools on wireline and logging-while-drilling sonic logging measurements. *Geophysical Prospecting*, 61:268–283, 2013.

T. J. Plona and D. L. Johnson. Experimental study of the two bulk compressional modes in water saturated porous structures. *Ultrasonic Symposium*, pages 864–872, 1980.

S. R. Pride and J. G. Berryman. Linear dynamics of double-porosity dual-permeability materials. i. governing equations and acoustic attenuation. *Physical Review*, 68:036603, 2003a.

S. R. Pride and J. G. Berryman. Linear dynamics of double-porosity dual-permeability materials. ii. fluid transport equations. *Physical Review*, 68: 036604, 2003b.

S. R. Pride, J. G. Berryman, and J. M. Harris. Seismic attenuation due to wave-induced flow. *Journal of Geophysical Research*, 109:B01201, 2004.

C. J. Randall. Multipole acoustic waveforms in nonaxisymmetric boreholes and formations. *Journal of Acoustical Society of America*, 90:1620–1631, 1991.

J. H. Rosenbaum. Synthetic microseismograms: logging in porous formations. *Geophysics*, 39(1):14–32, 1974.

M.S. Sams, J.P. Neep, M.H. Worthington, and M.S. King. The measurement of velocity dispersion and frequency-dependent intrinsic attenuation in sedimentary rocks. *Geophysics*, 62:1456–1464, 2017.

P. Sayar and C. Torres-Verdin. Effective medium modeling of velocity dispersion and attenuation in isotropic rocks. *Geophysics*, 82:D135–D156, 2017.

C. M. Sayers and M. Kachanov. Microcrack-induced elastic wave anisotropy of brittle rocks. *Journal of Geophysical Research*, 100:4149–4156, 1995.

D. P. Schmitt. Effects of radial layering when logging in saturated porous formations. *Journal of Acoustical Society of America*, 84:2200–2214, 1988a.

D. P. Schmitt. Shear wave logging in elastic formations. *Journal of Acoustical Society of America*, 84:2215–2229, 1988b.

D. P. Schmitt. Full wave synthetic acoustic logs in radially semiinfinite saturated porous media. *Geophysics*, 53:807–823, 1988c.

D. P. Schmitt. Shear-wave logging in semi-infinite saturated porous formations. *Journal of Acoustical Society of America*, 84:2230–2244, 1988d.

D. P. Schmitt. Acoustic multipole logging in transversely isotropic poroelastic formations. *Journal of Acoustical Society of America*, 86:2397–2421, 1989.

D. P. Schmitt. Dipole logging in cased boreholes. *Journal of Acoustical Society of America*, 93:640–657, 1993.

S. A. Shapiro. Elastic piezosensitivity of porous and fractured rock. *Geophysics*, 68:482–486, 2003.

B. K. Sinha. Sensitivity and inversion of borehole flexural dispersions for formation parameters. *Geophysical Journal International*, 128:84–96, 1997.

B. K. Sinha, E. Simsek, and Q. Liu. Elastic-wave propagation in deviated wells in anisotropic formations. *Geophysics*, 71(6):D191–D202, 2006.

R. D. Stoll. Acoustic waves in ocean sediments. *Geophysics*, 42:715–725, 1977.

R. D. Stoll and G. M. Bryan. Wave attenuation in saturated sediments. *Journal of Acoustical Society of America*, 47:1440–1447, 1969.

L. F. Sun, B. Milkereit, and N. Tisato. Analysis of velocity dispersion using full-waveform multichannel sonic logging data: A case study. *Geophysical Prospecting*, 64:1016–1029, 2016.

X. M. Tang and A. C. H. Cheng. *Quantitative borehole acoustic methods*. Elsevier Handbook of Geophysical Exploration. Seismic Exploration 24, 2004.

X. M. Tang, C. H. Cheng, and M. N. Toksöz. Dynamic permeability and borehole stoneley waves: A simplified biot-rosenbaum model. *Journal of Acoustical Society of America*, 90:1632–1646, 1991.

X. M. Tang, C. Li, and D. J. Patterson. A curve-fitting technique for determining dispersion characteristics of guided elastic waves. *Geophysics*, 75(3): E153–E160, 2010.

X. M. Tang, X. L. Chen, and X. K. Xu. A cracked porous medium elastic wave theory and its application to interpreting acoustic data from tight formations. *Geophysics*, 77(6):D245–D252, 2012.

B. D. Thompson, R. P. Young, and D. A. Lockner. Premonitory acoustic emissions and stick-slip in natural and smooth-faulted westerly granite. *Journal of Geophysical Research*, 114:B02205, 2009.

B. W. Tichelaar and K. W. van Luik. Sonic logging of compressional-wave velocities in a very slow formation. *Geophysics*, 9:1627–1633, 1995.

L. Tsang and R. Rader. Numerical evaluation of the transient acoustic waveform due to a point source in a fluid filled borehole. *Geophysics*, 44:1706–1720, 1979.

J. E. White. The hula log: A proposed acoustic tool, 1967.

J. E. White and C. Tongtaow. Cylindrical waves in transversely isotropic media. *Journal of Acoustical Society of America*, 70:1147–1155, 1981.

G. A. Winbow. A theoretical study of acoustic S-wave and P-wave velocity logging with conventional and dipole sources in soft formations. *Geophysics*, 53(10):1334–1342, 1988.

K. W. Winkler. Dispersion analysis of velocity and attenuation in berea sandstone. *Journal of Geophysical Research*, 90:6793–6800, 1985.

J. Yang, B. Sinha, and T. M. Habashy. Estimation of formation shear and borehole-fluid slownesses using sonic dispersion data in well-bonded cased boreholes. *Geophysics*, 76(6):E187–E197, 2011.

L. Zhang. Aspects of rock permeability. *Frontiers of Structural and Civil Engineering*, 7:102–116, 2013.

Vita

Elliot Dahl was born in Stockholm, Sweden in January 1986. He obtained a B.S. degree in Engineering Physics in 2010 and M.S. degree in Applied Mathematics from KTH, Royal Institute of Technology in Stockholm, Sweden in 2013. In August 2013, he entered the Jackson school of Jackson School of Geosciences at the University of Texas at Austin as a Ph.D. student.

Email: elliotdahl@utexas.edu

This dissertation was typed by Elliot Dahl.

This dissertation was typeset with LaTeX[†] by the author.

[†]LaTeX is a document preparation system developed by Leslie Lamport as a special version of Donald Knuth's TeX Program.